



## Global vegetation, moisture, thermal and climate interactions intensify compound extreme events



Oluwafemi E. Adeyeri <sup>a,b,d</sup>, Wen Zhou <sup>b,c,\*</sup>, Christopher E. Ndehedehe <sup>d,e</sup>, Xuan Wang <sup>a</sup>

<sup>a</sup> Low-Carbon and Climate Impact Research Centre, School of Energy and Environment, City University of Hong Kong, Kowloon, Hong Kong

<sup>b</sup> Key Laboratory of Polar Atmosphere-Ocean-Ice System for Weather and Climate, Ministry of Education, Department of Atmospheric and Oceanic Sciences, Institute of Atmospheric Sciences, Fudan University, Shanghai, China

<sup>c</sup> Key Laboratory for Polar Science of the MNR, Polar Research Institute of China, Shanghai, China

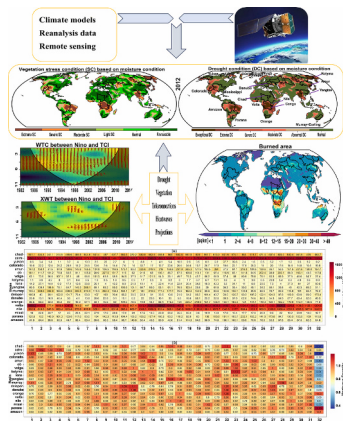
<sup>d</sup> Australian Rivers Institute, Griffith University, Nathan, QLD 4111, Australia

<sup>e</sup> School of Environment and Science, Griffith University, Nathan, QLD 4111, Australia

### HIGHLIGHTS

- Heatwave severity facilitated wildfire development by drying out dead fine fuel.
- Unfavorable thermal conditions intensified heatwave severity.
- Moisture and vegetation density abated heatwave severity in most basins.
- Drought absence does not guarantee favorable vegetation states.
- Lowest VCI, VHI, and TCI in the Murray-Darling basin during the Australian drought

### GRAPHICAL ABSTRACT



### ARTICLE INFO

Editor: Paulo Pereira

**Keywords:**

Compound extreme events  
Climate change adaptation

### ABSTRACT

Compound extreme events, encompassing drought, vegetation stress, wildfires, and heatwave severity, and heatwave intensity (CDVWHS), pose significant threats to societal, environmental, and health systems. Understanding the intricate relationships governing CDVWHS evolution and their interaction with climate teleconnections is crucial for effective climate adaptation strategies. This study leverages remote sensing, reanalysis data, and climate models

**Abbreviations:** CDVWHS, Compound drought, vegetation stress, wildfires, and heatwave severity; SSP, Shared Socioeconomic Pathways; VCI, Vegetation Condition Index; VHI, Vegetation Health Index; VHIs, Vegetation Health Indicators; NDVI, Normalized Difference Vegetation Index; ENSO, El Niño Southern Oscillation; GCM, General Circulation Models; AVHRR, Advance Very High-Resolution Radiometer; LTDR, Long Term Data Record; CMIP6, Coupled Model Intercomparison Project Phase 6; PNA, Pacific/North American teleconnection pattern; TNA, Tropical Northern Atlantic Index; NAO, North Atlantic Oscillation; NP, North Pacific Index; DMI, Dipole Mode Index; NINO, Niño 3.4 SST Index; CPC, Climate Prediction Centre; DC, Drought Conditions; EHF, Excess Heat Factor; CWT, Continuous Wavelet Transform; XWT, Cross Wavelet Transform; WTC, Wavelet Coherence; CCS, Climate Change Signals; TCI, Temperature Condition Index.

\* Corresponding author.

E-mail address: [wen\\_zhou@fudan.edu.cn](mailto:wen_zhou@fudan.edu.cn) (W. Zhou).

Wildfires  
Heatwaves  
Vegetation stress  
Drought

to analyze CDVWHS during historical (1982–2014), near-future (2028–2060), and far-future (2068–2100) periods under two Shared Socioeconomic Pathways (SSP; 245 and 585). Our results show that reduced vegetation health, unfavorable temperature conditions, and low moisture conditions have negligible effects on vegetation density. However, they worsen the intensity of heatwaves and increase the risk of wildfires. Wildfires can persist when thermal conditions are poor despite favorable moisture levels. For example, despite adequate moisture availability, we link the 2012 Siberian wildfire in the Ob basin to anomalous negative thermal conditions and concurrent unfavorable thermal-moisture conditions. In contrast, the Amazon experiences extreme and exceptional drought associated with unfavorable moisture conditions in the same year. A comparative analysis of Siberian and North American fires reveals distinct burned area anomalies due to variations in vegetation density and wildfire fuel. The North American fires have lower positive anomalies in burned areas because of negative anomalous vegetation density, which reduced the amount of wildfire fuel. Furthermore, we examine basin-specific variability in climate teleconnections related to compound CDVWHS, revealing the primary modes of variability and evolution of CDVWHS through climate teleconnection patterns. Moreover, a substantial increase in the magnitude of heatwave severity emerges between the near and far future under SSP 585. This study underscores the urgency for targeted actions to enhance ecosystem resilience and safeguard vulnerable communities from CDVWHS impacts. Identifying CDVWHS hotspots and comprehending their complex relationships with environmental factors are essential for developing effective adaptation strategies in a changing climate.

## 1. Introduction

Climate change is increasingly associated with the rising frequency and severity of extreme climatic events, such as droughts and heatwaves, that pose threats to ecosystems, agriculture, and human health (Adeyeri et al., 2019; Adeyeri et al., 2023a; AghaKouchak et al., 2014; Ballarin et al., 2021; Nairn et al., 2018). Heatwaves, which are prolonged periods of exceptionally high temperatures, are one of the most prominent examples of such events, as they have become more frequent and intense due to climate change (Adeyeri et al., 2022b; Jyoteeshkumar reddy et al., 2021a; Perkins-Kirkpatrick and Lewis, 2020). The heat index, which combines temperature and humidity to measure the perceived level of heat by the human body (also known as *human thermal comfort*), is strongly influenced by the atmospheric moisture content, mainly water vapor (Adeyeri et al., 2023b; Steadman, 1979). High humidity levels can impair the effectiveness of evaporative cooling, making it harder for people and animals to regulate their body temperature (Sherwood and Huber, 2010). This can result in different levels of heatwave severity and human thermal discomfort (Adeyeri et al., 2023b; Nairn and Fawcett, 2013). Moreover, the complex interaction between humidity and temperature plays a significant role in heatwave dynamics. Heatwaves are often related to high-pressure systems that create atmospheric blocking patterns (Lau and Nath, 2014), which trap moisture, increase humidity, decrease cloud cover, and raise surface temperatures (Dole et al., 2011). In some cases, increased evapotranspiration from higher temperatures can dry out the soil, reducing the cooling effect of evaporation and intensifying heatwaves (Fischer et al., 2007). These effects on soil moisture can cause water shortage (soil moisture drought).

Drought is a complex environmental hazard that occurs when precipitation is insufficient for a prolonged period, resulting in water scarcity that affects ecosystems, agriculture, and humanity (Wilhite and Glantz, 1985). Drought can be classified into three types: (i) meteorological drought, which is a deviation of precipitation from the long-term average of a region; (ii) agricultural drought, which is a deficiency of soil moisture for crop and vegetation water needs; and (iii) hydrological drought, which is a depletion of water in streams, rivers, lakes, and groundwater systems. Drought occurrence and severity depend on temperature, moisture availability, and their interactions (Trenberth et al., 2014). Human-induced climate change increases the risk of higher evapotranspiration rates and soil moisture deficits as global temperatures rise (Sheffield et al., 2012). The resulting decrease in available moisture can aggravate drought conditions, leading to more frequent and severe events (Adeyeri et al., 2023a; Dai, 2011). Drought and plant stress are directly related, as water availability is essential for plant growth and yield (Farooq et al., 2009). Prolonged water deficit can cause stomatal closure, reduced photosynthesis and plant death

(Adeyeri and Ishola, 2021; Chaves et al., 2003; Teixeira et al., 2013).

Temperature and drought frequency are projected to increase vegetation stress and reduce agricultural production in many regions (Reichstein et al., 2013; Seneviratne et al., 2006). During droughts, low water availability induces stress in plants and ecosystems, leading to poor vegetation health, wilting, browning, and death. Consequently, dry conditions and stressed or dead vegetation create ideal fuel for wildfires, threatening landscapes like forests and grasslands. Moisture conditions, such as precipitation and soil moisture content, mainly determine water accessibility to ecosystems and agriculture. However, changes in precipitation patterns significantly affect drought conditions, while soil moisture content is crucial in determining vegetation stress and its response to heatwaves (Allen et al., 2010). Moreover, moisture conditions interact with other environmental factors, such as temperature and humidity, amplifying drought impacts and worsening stress on vegetation and agriculture (Adeyeri et al., 2024; Diffenbaugh and Ashfaq, 2010).

Therefore, moisture and thermal conditions shape the Earth's climate and ecosystems, influencing drought, vegetation stress, and heatwave severity. These factors, in turn, have profound implications for agriculture, ecosystems, and human health. For example, a strong inverse relationship was found between precipitation and heatwave severity in Australia, where higher rainfall leads to shorter and less intense heatwaves (Perkins and Alexander, 2013). A similar pattern was observed in the central and eastern United States, where more precipitation correlates with lower heatwave severity (Diffenbaugh and Ashfaq, 2010). This effect was attributed to increased soil moisture and evaporative cooling (Diffenbaugh and Ashfaq, 2010), with a more pronounced impact in regions where soil moisture is a limiting factor for evapotranspiration, such as semi-arid and arid environments (Miralles et al., 2014).

However, it is important to note that heatwaves can also worsen drought conditions, as high temperatures increase evaporation rates, leading to further drying of soils and vegetation. Therefore, understanding the complex relationships between moisture and thermal conditions and their cascading impacts is essential for developing effective strategies to mitigate adverse effects. In recent decades, various drought indices have been developed and applied to classify different types of drought (Adeyeri et al., 2023a; Ault, 2020; Cheng et al., 2023; Derradji et al., 2023; Mukhwana et al., 2023; Ndehedehe et al., 2023b; Nugraha et al., 2023). For example, the Multivariate Standardized Drought Index combines the Standardized Precipitation Index, the Standardized Soil Moisture Index, and the Standardized Runoff Index, which use precipitation, soil moisture, and runoff data to provide insights into meteorological, soil moisture, and hydrological drought conditions, respectively (Adeyeri et al., 2023a; Hao and AghaKouchak, 2013). Also, the Standardized Precipitation Evapotranspiration Index,

which uses precipitation and evapotranspiration data, has been used to characterize meteorological drought (Ndehedehe et al., 2023b; Vicente-Serrano et al., 2010a; Vicente-Serrano et al., 2010b). However, these indices often measure how much a moisture variable deviates from its historical normal distribution. Despite this, different drought indicators result in changes in drought events and characteristics (Adeyeri et al., 2023a; Dai, 2013).

The Vegetation Condition Index (VCI), Temperature Condition Index (TCI), and Vegetation Health Index (VHI), which have been widely used to monitor and detect drought-related vegetation conditions, were proposed as a new type of satellite-based drought index to describe the cumulative moisture, temperature, and vegetation health conditions, respectively (Jiang et al., 2021; Kogan et al., 2012; Kogan et al., 2013; Pei et al., 2018). These Vegetation Health Indicators (VHIs) overcome the limitations of standard drought monitoring tools and indices as they incorporate land surface characteristics with drought conditions (Kogan et al., 2013). These satellite-based VHIs are emerging as important drought metrics, given their broad application in characterizing drought-affected areas as well as the magnitude of drought impacts on vegetation growth, crop productivity, wildfire regimes, and water resources (Abdulla-Al et al., 2023; Bento et al., 2018; Bokusheva et al., 2016; Jiang et al., 2021; Kogan, 1990; Parente et al., 2019; Pei et al., 2018; Weng et al., 2023; Yang et al., 2018; Yang et al., 2020). However, gaps remain in understanding the moisture-thermal connection and its influence on compound drought, vegetation stress, wildfires, and heatwave severity (CDVWHS). Additionally, the role of various climate teleconnection patterns in driving concurrent drought impacts and vegetation stress has been largely ignored. While Zhao et al. (2018) associated the interannual variability of the Normalized Difference Vegetation Index (NDVI) during the growing season with El Niño Southern Oscillation (ENSO), Aboka and Mishra (2015) predicted vegetation health by analyzing the relationship between Niño 3.4 and NDVI over India, Erasmi et al. (2014) attributed reduced vegetation greenness to ENSO warm events in Northern Brazil, and Jiang et al. (2021) established a positive correlation between TCI and Niño 3.4, the climate teleconnection effects vary for different regions. Therefore, a comprehensive global assessment of the compound event is imperative.

This study, therefore, investigates the intricate relationships among compound drought, vegetation stress, wildfires, and heatwave severity at both global and basin scales, using indices related to moisture, thermal conditions, and climate teleconnections. Additionally, we aim to explore how these factors jointly affect drought, wildfires, vegetation stress, and heatwave severity. Given the potential role of climate teleconnections in driving variability in surface vegetation greenness, this study adopts a holistic approach by further investigating the impact of six different climate teleconnection patterns on compound drought, vegetation stress, wildfires, and heatwave severity (CDVWHS). To this end, we analyze (1) the spatiotemporal variations of VHIs - TCI (a proxy for thermal condition), VCI (a proxy for moisture condition), VHI (a proxy for the combined effect of thermal and moisture condition), burned area (from wildfires) and heatwave severity derived from satellite, reanalysis and climate models, (2) the trend of CDVWHS, (3) the basin-scale CDVWHS sensitivity to climate teleconnections using wavelet analysis and, (4) the future projection of heatwave severity using the multi-model ensemble mean of ten general circulation models (GCM) models under two climate change scenarios.

## 2. Data and methods

### 2.1. Data

We derive the satellite-based vegetation health indicators from the Advance Very High-Resolution Radiometer (AVHRR, Supplementary Table S1) NDVI3g monthly time series product (Pinzon and Tucker, 2014), spanning from 1981 to 2015 at a spatial resolution of ~8 km and the monthly brightness temperature from the Japanese 55-year

Reanalysis (JRA55, <http://rda.ucar.edu/datasets/ds628.1/>), at 1° resolution (Kobayashi et al., 2015). We estimate the burnt area using the monthly spectral data from the AVHRR Land Long Term Data Record (LTDR) product version 5, which spans from 1982 to 2018 at a 0.25° grid resolution (Chuvieco et al., 2020). We excluded 1994 from the dataset because the LTDR Archive did not provide sufficient data for that year. We analyze the burned areas based on the active fire season, i.e., May to April for the northern hemisphere and November to October for the southern hemisphere (Richardson et al., 2022). This is important for establishing the lagged relationship between VHIs and wildfire. We estimate the heatwave severity projection based on the multi-model ensemble mean of ten Coupled Model Intercomparison Project Phase 6 (CMIP6) GCMs (Supplementary Table S2) under two shared socioeconomic pathways (SSP 245 and 585) during the near future (2028–2060) and far future (2068–2100). SSP 245 is based on the implementation of climate protection measures. It suggests a radiative force of 4.5 W/m<sup>2</sup> by 2100 (O'Neill et al., 2016), while SSP585 is the only SSP with emissions sufficient to deliver the 8.5 W/m<sup>2</sup> level of forcing in 2100. Subsequently, we aggregate the monthly fields to extended summer seasons in the northern and southern hemispheres. All datasets are regridded to a standard 1° × 1° grid using the bilinear interpolation technique to prevent erroneous scale gap effects (Adeyeri et al., 2022b). The wavelet plots are based on the spatial mean aggregation of the basins. To unify the study period while avoiding the overlap of the historical period with future climate scenarios, which started in 2015, the historical period is restricted to between 1982 and 2014. The teleconnection datasets include the Pacific/North American teleconnection pattern (PNA), Tropical Northern Atlantic Index (TNA), North Atlantic Oscillation (NAO), North Pacific Index (NP), Dipole Mode Index (DMI), and Niño 3.4 SST Index (NINO) (Supplementary File, Section 1). These are retrieved from the National Weather Service Climate Prediction Centre (CPC) archives of NOAA and are available at <https://www.cpc.ncep.noaa.gov/data/indices/>, [https://psl.noaa.gov/gcos\\_wgsp/Timeseries/DMI/](https://psl.noaa.gov/gcos_wgsp/Timeseries/DMI/), and <https://stateoftheoceanoceanscience.noaa.gov/sur/>.

### 2.2. Methods

#### 2.2.1. Satellite-based VHIs and change signal

NDVI is the ratio of the difference between the reflectance measured in the near-infrared region of the electromagnetic spectrum and the reflectance observed in the red portion of the electromagnetic spectrum. However, NDVI has low sensitivity to vegetation red edge, which reflects slight differences in gap fractions, canopy leaf content, and senescence (Adeyeri et al., 2017), making it difficult to adapt to different ecosystems (Kogan, 1990). Nonetheless, stratifying NDVI permits evaluating the effects of weather on vegetation in non-homogeneous locations, resulting in VCI. VCI indicates vegetation response to precipitation because it is more responsive to rainfall dynamics than NDVI (Kogan, 1990); hence, it quantifies water-related vegetation stress.

VCI is given as:

$$VCI = 100 * \frac{[NDVI - NDVI_{min}]}{[NDVI_{max} - NDVI_{min}]} \quad (1)$$

where  $NDVI_{min}$  and  $NDVI_{max}$  are the multi-year absolute minimum and maximum NDVI, respectively.

On the other hand, TCI quantifies temperature-related vegetation stress, while VHI combines the weighted averages of VCI and TCI. VHI quantifies the combined effect of water and temperature-related vegetation stress.

TCI is given as:

$$TCI = 100 * \frac{[BT_{max} - BT]}{[BT_{max} - BT_{min}]} \quad (2)$$

where  $BT_{min}$  and  $BT_{max}$  are the multi-year absolute minimum and maximum brightness temperatures, respectively.

$$VHI = [1 - \beta]^*TCI + \beta^*VCI \quad (3)$$

where  $\beta$  quantifies the contribution of moisture and temperature to the overall vegetation health. The weight  $\beta$  is 0.5 (Kogan, 1990). Generally, higher values imply better moisture, thermal, and vegetation states (Jiang et al., 2021; Kogan et al., 2013). They also provide precise information about identifying and tracking drought and vegetation stress severity. Therefore, we evaluate the cumulative moisture, temperature, and vegetation health components using the VCI, TCI, and VHI, respectively.

### 2.2.2. Partial correlation

The partial correlation becomes crucial when several factors impact a phenomenon (Adeyeri et al., 2022b). A relationship is partial when two variables are linked, but a third or multiple other elements operate as conditions (Adeyeri et al., 2022b; Adeyeri et al., 2024; Kim, 2015; Ndehedehe et al., 2023a). We assess the monotonic relationship among the CDVWHS variables using the Spearman correlation because of the varying variance and linearity of the CDVWHS events (Adeyeri et al., 2022b).

The partial correlation of variables  $A$ ,  $B$ , and  $C$  is:

$$\rho_{ABC} = \frac{\rho_{AB} - \rho_{AC}\rho_{BC}}{\sqrt{(1 - \rho^2_{AC})^*(1 - \rho^2_{BC})}} \quad (4)$$

For a set of  $n$  controlled variables,  $C$  is

$$C = \{C_1, C_2, \dots, C_n\}$$

### 2.2.3. Drought and vegetation stress classification

We classify drought and vegetation stress levels by different thresholds based on the VHIs values. VHIs between 0 and 5 indicate exceptional drought conditions (DC); between 6 and 15, extreme DC; between 16 and 25, severe DC; between 26 and 35, moderate DC; between 36 and 40, abnormal DC; and above 40, normal condition. Low VCI, TCI, or VHI values reflect unfavorable moisture, thermal conditions, or a combination of both conditions, which are indicators of or contributors to drought development, as classified by specific thresholds applied to the indices. Similarly, VHIs between 0 and 10 indicate extreme vegetation stress condition (SC); between 11 and 20, severe SC; between 21 and 35, moderate SC; between 36 and 40, light SC; between 41 and 60, normal, and above 60, favorable.

### 2.2.4. Trends and evolution

We analyze the VHIs evolutionary trajectory from 1982 to 2014. We examine nineteen discrete basins, enabling a thorough understanding of the fluctuations and progression of the VHIs signal within the spatio-temporal domain. We use the modified Mann-Kendall statistics (Adeyeri et al., 2022b; Adeyeri et al., 2024; Kendall, 1948; Mann, 1945) to estimate the global spatial trend and the Theil-Sen slope (Adeyeri et al., 2024; Sen, 1968; Theil, 1992) to measure the magnitude of the trends. The details of this method are presented in the Supplementary File, Section 2.

### 2.2.5. Cross wavelet transform, wavelet coherence, and climate modes

To investigate the relationship between the climate teleconnections and CDVWHS, we apply the wavelet analysis method, which can capture the periodic fluctuations and local features of the signals. The combined time-frequency wavelet decomposition approach using the Morlet continuous wavelet transform (CWT) has been proven reliable for analyzing such signals (Abolfazl and Gurdak, 2020; Adeyeri et al., 2020a; Ng and Chan, 2012; Torrence and Webster, 1999; Veleda et al., 2012). This approach disassembles signals, enabling the representation of signal trends and specifics over time ranges and demonstrating transitory and localized behavior (Adeyeri et al., 2020a; Ndehedehe et al., 2023a; Torrence and Webster, 1999). In this transformation, a two-parameter basis  $\{\psi_{a,\tau}(t), (a, \tau) \in (\mathbb{R}_+^* \times R)\}$  replaces the Fourier

basis, where ' $\tau$ ' is the shift in time and ' $a$ ' is the scale. The Fourier basis depicts a signal in terms of the power and frequency of its decomposed sine waves, but disregards its time. However, this modification aids timeframe discrimination during analysis (Adeyeri et al., 2020a). The continuous-time signal  $x(t)$  in the transform has coefficients which are defined by a linear integral operator:

$$C_x(a, \tau) = \int_{-\infty}^{+\infty} x(t) \psi_{a,\tau}^*(t) dt \quad (5)$$

where  $\psi_{a,\tau}^*(t) = \frac{1}{\sqrt{a}} \psi(\frac{t-\tau}{a})$ , \* is the complex conjugate and  $\psi(t)$  is the wavelet.

The wavelet power spectrum of the variables' local covariances is generated by the wavelet energy stress of the time series across multiple scales. This transform deconstructs complicated signals into fundamental signals of finite bandwidth without affecting the primary signal's phases (Adeyeri et al., 2020a; Adeyeri and Ishola, 2021; Ndehedehe et al., 2023a). Moreover, the wavelet coherence between variables can unveil the climate processes or weather systems that influence vegetation stress, drought, and other auxiliary variables at different scales (Adeyeri et al., 2020a; Adeyeri and Ishola, 2021; Ndehedehe et al., 2023a). Therefore, we implement the wavelet coherence to identify the climate processes influencing CDVWHS on each timescale. Subsequently, we utilize the Cross Wavelet Transform (XWT), which consists of two CWTs, to find areas in time and frequency space where both time series exhibit high common power.

The covariance of the two time series  $A$  and  $B$  using XWT is given as:

$$W_m^{AB} = W_m^A[s] \times W_m^B[s] \quad (6)$$

where  $m$  and  $s$  are the time and scale of the wavelet transform,  $W_m^A[s]$  and  $W_m^B[s]$  are  $A$  and  $B$  wavelet transforms, respectively, and  $W_m^B[s]$  is the complex conjugation of  $W_m^B[s]$ . The phase relationships between  $A$  and  $B$  in time and frequency phase is denoted by  $W_m^{AB}$ .

We eliminate the bias problem associated with low-frequency oscillations in the wavelet power spectra (Ng and Chan, 2012; Veleda et al., 2012) by bias-correcting the power and normalizing it by the variance (Adeyeri and Ishola, 2021; Liu et al., 2007). We utilize Wavelet Coherence (WTC) to pinpoint the necessary coherence between two CWTs, irrespective of whether the two time series possess high mutual powers.

The WTC is given as:

$$R_m^2(s) = \frac{|SM \langle s^{-1} W_m^{AB}(s) \rangle|^2}{SM \langle s^{-1} |W_m^A(s)|^2 \rangle SM \langle s^{-1} |W_m^B(s)|^2 \rangle} \quad (7)$$

where  $SM$  is the smoothing operator,  $\langle \rangle$  smooths the wavelet spectrum at different scales and time,  $R_m^2(s) \in [0, 1][0, 1]$ .

$$SM = SM_{scale}[SM_{time}(W_n(s))]$$

$SM_{scale}$  and  $SM_{time}$  smooths along the scale and time axes, respectively.

$$SM_{time}(W)|_m = \left[ W(t, s) c_2 \prod (0.6s) \right] |_m$$

$$SM_{scale}(W)|_s = \left[ W(t, s) c_1 e^{-\left(\frac{s^2}{2c^2}\right)} \right] |_s$$

where  $C1, C2$  are the normalized constants, 0.6 is the Morlet wavelet empirical decorrelation length,  $\prod$  is the rectangular function.

The wavelet phase angle is:

$$\varnothing_m(s) = \tan^{-1} \left[ \frac{\{\langle s^{-1} W_m^{AB}(s) \rangle\}^* \alpha}{\{\langle s^{-1} W_m^{AB}(s) \rangle\}^* \beta} \right]$$

where  $\{\langle s^{-1} W_m^{AB}(s) \rangle\}^*\alpha$  and  $\{\langle s^{-1} W_m^{AB}(s) \rangle\}^*\beta$  are the wavelet spectra's imaginary and real parts, respectively.

The relative phase relationship is depicted using arrows: arrows pointing right (left) indicate in-phase (anti-phase) correlation. The cone of influence demarcates the area of the wavelet spectrum where edge effects become significant; it also indicates where the wavelet power dropped for edge discontinuity, implying that edge effects become insignificant beyond this point. However, it is essential to note that edge effects inside and outside the cone of influence cannot be ignored since the wavelet is not fully localized over the study period (Torrence and Webster, 1999). The WTC and XWT between CDVWHS and different atmospheric teleconnections (as explained in the supplementary file) are investigated using wavelets, respectively.

#### 2.2.6. Heatwave severity and climate change signal

Intense heatwaves harm human and plant health (Adeyeri et al., 2022a; Jyoteeshkumar reddy et al., 2021a; Nairn and Fawcett, 2013). Therefore, we classify heatwaves from the low to the severe, identifying occurrences with more significant health implications (Jyoteeshkumar reddy et al., 2021a). The heatwave severity is given as (Nairn and Fawcett, 2013):

$$\text{Severity} = \frac{E\text{HF}}{E\text{HF}_{85p}} \quad (8)$$

$$\text{Heatwave} = \begin{cases} \text{Low - Intense heatwave, } 0 \leq \text{Severity} < 1 \\ \text{Severe heatwave, } \text{Severity} \geq 1 \end{cases} \quad (9)$$

The 85th percentile of positive excess heat factor (EHF) values for the complete study period at a particular domain is denoted by  $E\text{HF}_{85p}$ . We calculate EHF using a three-day averaged daily temperature compared to the 95th percentile of climatological temperatures and the recent

(previous 30-day) temperatures (Adeyeri et al., 2022a; Perkins et al., 2015). Therefore, a heatwave is defined as three or more days with positive EHF.

$$E\text{HF} = E\text{HI}_{\text{sig}} * \max[E\text{HI}_{\text{acc}}, 1]$$

where

$$E\text{HI}_{\text{sig}} = \frac{[T_k + T_{k-1} + T_{k-2}]}{3} - T_{90}, \quad E\text{HI}_{\text{acc}} = \frac{[T_k + T_{k-1} + T_{k-2}]}{3} - \frac{[T_{k-3} + \dots + T_{k-32}]}{30} \quad \text{and} \\ T = \frac{[T_{\text{max}} + T_{\text{min}}]}{2}. \quad T_{90} \text{ is the climatological 90th percentile temperature during the base period (1982–2010), } T, T_{\text{min}}, T_{\text{max}}, \text{ and } T_k \text{ denote the daily mean air, minimum, maximum, and } k^{\text{th}} \text{ day daily mean temperatures, respectively. } T_{90} \text{ is computed for each day of the year for the specific base period using a 15-day centered window and smoothed with a Savitzky-Golay third-order polynomial filter (Jyoteeshkumar reddy et al., 2021a). The } E\text{HF} \text{ calculation's window-based daily relative threshold technique enables the year-round capture of all variations in heatwave metrics. } E\text{HI}_{\text{acc}} \text{ is the current 3-day temperature variance relative to the prior month's average temperature; } E\text{HI}_{\text{sig}} \text{ represents the divergence of the current 3-day period temperature from the climatological relative threshold.}$$

To facilitate risk management, climate projections should encompass various plausible future climate change scenarios (Adeyeri et al., 2022b). Thus, we quantify the climate change signal (CCS) in heatwave severity by calculating the difference between (i) the far future and the historical period, (ii) the near future and the historical period, and (iii) the far future and the near future. Fig. 1 illustrates the complete methodology flowchart.

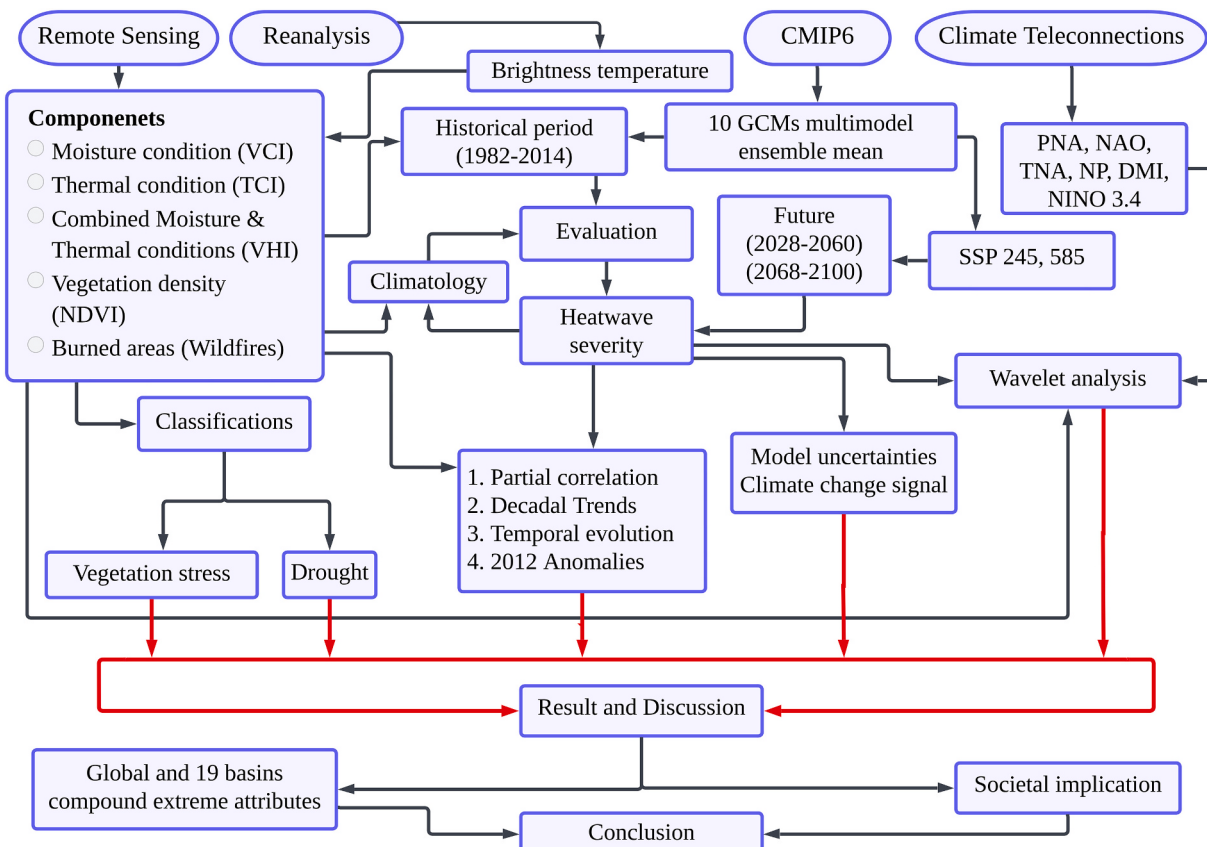


**Fig. 1.** Methodology flow chart of the study.

### 3. Results and discussion

#### 3.1. CDVWHS spatial distribution and change signal

Understanding and managing the risks associated with compound extreme events is crucial for building resilience in the face of climate change. These events interact in complex ways, resulting in interrelated consequences. Therefore, this section highlights the importance of understanding these compound extremes. The long-term average VCI from 1982 to 2014 in the Congo, Amazon, Danube, Dnieper, Parana, and Volta basins range from 40 to 90 %, indicating favorable moisture conditions (Fig. 2a). These conditions, along with optimal thermal conditions (Fig. 2c), trigger excellent vegetation health (50–90 %), especially in the Congo basin (Fig. 2b). Additionally, the severity of heatwaves is relatively low (<0.87, Fig. 2d) due to the excellent vegetation health and high vegetation density (0.7–0.9, Fig. 2e). Previous studies have shown that vegetation reduces heat intensities (Adeyeri et al., 2024; Ossola et al., 2021), and that vegetated areas also contribute to cooling during heatwaves through evapotranspiration (Adeyeri and Ishola, 2021; Adeyeri et al., 2024; Liu et al., 2021). On the other hand, basins like Lena experience limited moisture, suboptimal thermal conditions, and reduced vegetation health. However, this only slightly affects vegetation density, while the severity of heatwaves remains notably high. Similarly, the western part of the Amazon basin is generally associated with low moisture levels, suboptimal thermal conditions, and vegetation health. Surprisingly, this does not translate to low vegetation density, as this may depend on the vegetation type and foliage properties. However, heatwave severity is more pronounced in this region than in others. Regarding the extent of wildfire-induced burned areas, the Congo, Chad, Nile, and Volta basins exhibit the largest burned areas, ranging from 1 to over 40 km<sup>2</sup> (Fig. 2f). This may be due to various land use and farm practices (Adeyeri et al., 2023b; Yu et al., 2022) and the challenges in combating wildfires in such regions. Due to their rich vegetation density, these areas tend to have more fuel to facilitate wildfires, leading to higher fire carbon emissions (Yu et al.,

2022). Climate change has further exacerbated the situation, resulting in faster drying across tropical regions (Cook et al., 2020; Zhou et al., 2014) and an increased frequency of severe tropical drought (Adeyeri et al., 2023a; Morales et al., 2020).

We also illustrate the CDVWHS change signal from 1982 to 2014 (Fig. S1). We note stronger moisture signals in all basins except the Amazon, Congo, and Parana in 2014 (Fig. S1a). In contrast, most African basins experienced a stronger signal from the combined influence of moisture and thermal conditions in 1982 (Fig. S1b). Notably, basins with a strong combined signal from moisture and thermal conditions in 1982 (negative VHI values), such as the Parana and Congo basins, also exhibit a stronger thermal signal (negative TCI values; Fig. S1c). Moreover, there is a rise in the severity of heatwaves across most regions (Fig. S1d), which is attributed to the impact of climate change (Adeyeri et al., 2022b; Jyoteeshkumar reddy et al., 2021a; Perkins-Kirkpatrick and Lewis, 2020). However, a reduction in vegetation density across most rainforests (including the Amazon, Congo, and Parana basins; Fig. S1e) suggests a possible shift in land use from primary to secondary forest (Adeyeri et al., 2023b). Furthermore, burnt areas increased by at least 6 km<sup>2</sup> in 2014 compared to 1982 (Fig. S1f). Nonetheless, suboptimal thermal, moisture conditions, or a combination of both can rapidly deteriorate vegetation health, leading to increased heatwave severity (reduced cooling effects) and more wildfires (Allen et al., 2021; Pincetl et al., 2019).

#### 3.2. Partial correlation among CDVWHS variables

We implement a partial correlation to assess the relationship among CDVWHS variables due to the unclear climatological spread pattern. Fig. 3a shows a predominantly positive partial correlation between heatwave severity and burned areas in the Congo, Yangtze, and Volga basins. This suggests that heatwave severity contributes to wildfire spread in such areas due to vegetation dead fine fuel dryness or lower dead fine fuel moisture content (Jyoteeshkumar reddy et al., 2021b; Mateus and Fernandes, 2014; Pausas and Paula, 2012). Furthermore, the

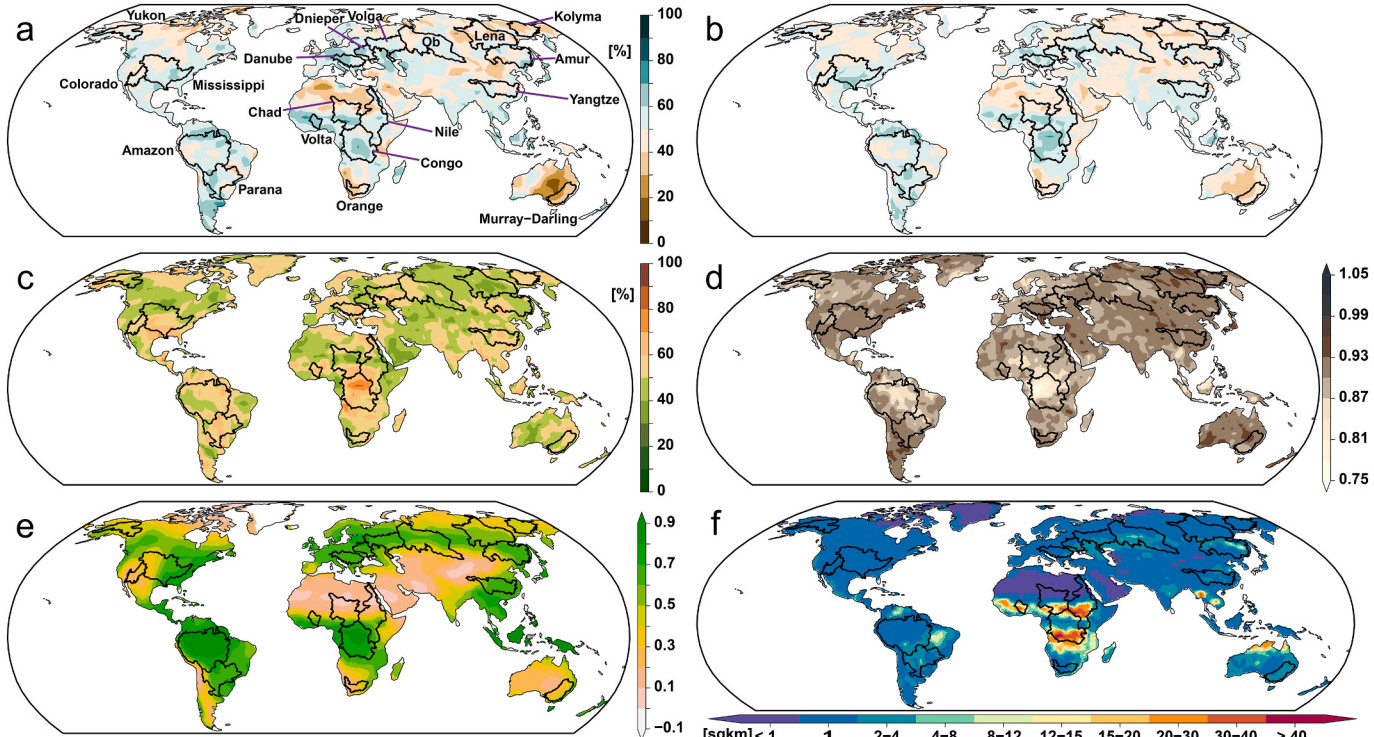


**Fig. 2.** Long-term average state from 1982 to 2014 of (a) VCI, (b) VHI, (c) TCI, (d) heatwave severity, (e) vegetation density, (f) burned area. The black polygons represent basins.

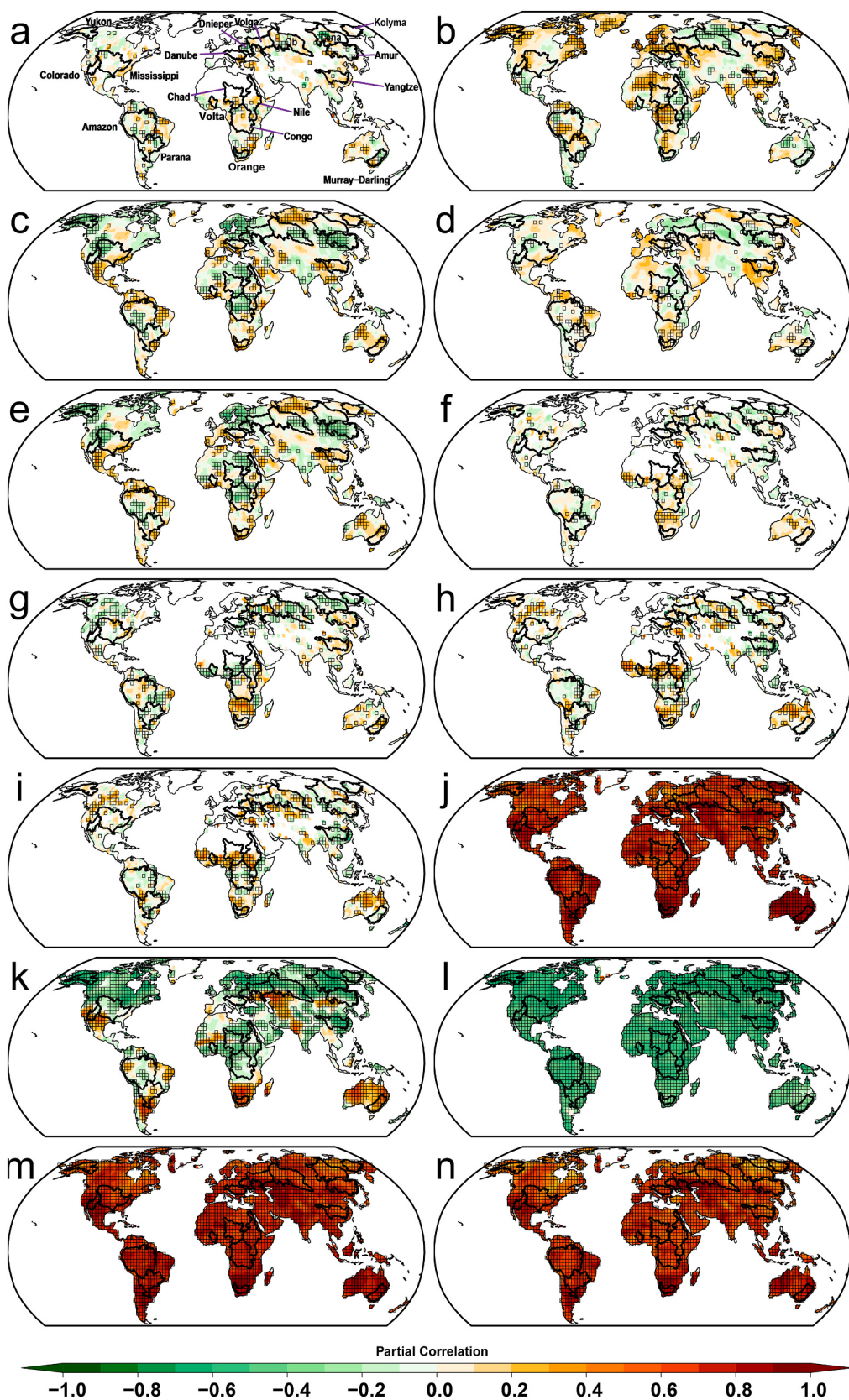


**Fig. 3.** Partial correlation of heatwave severity with (a) burned area, (b) TCI, (c) VCI (d) VHI (e) vegetation density; burned areas with (f) VHI, (g) TCI, (h) VCI, (i) vegetation density; TCI with (j) VHI, (k) VCI, (l) vegetation density; VCI with (m) VHI, and VHI with (n) vegetation density. Hatching represents significant correlations at a 95 % confidence level. The black polygons represent basins.

relationship between heatwave severity and TCI is notably strong in most basins (Fig. 3b). Except for the Murray-Darling, Kolyma, Ob, and Volga basins, all other basins exhibit high positive correlations, indicating that thermal conditions significantly influence the severity of heatwaves in those regions. However, basins with negative correlations suggest that factors other than thermal conditions also contribute to the severity of heatwaves in those areas. For example, the combined effects of divergent conditions in vertically integrated moisture flux and an unusual anticyclonic circulation hinder moisture inflow (Drumond et al., 2017), thereby leading to a severe heatwave, reduction in groundwater levels, and impacts on the overall functioning of ecosystems (Peñuelas et al., 2017).

Fig. 3c hints that moisture abates heatwave severity in the Congo, Amur, and Yukon basins; however, an increase (decrease) in heatwave severity corresponds to an increase (decrease) in moisture content in the Murray-Darling, Yantze, Orange, and Kolyma basins, signifying the contradictory contributions of moisture availability to heatwave severity (Adeyeri et al., 2024; Evan et al., 2015). Moreover, the net radiation budget at the ground surface provides physical reasons for this phenomenon. When the soil is wet, the latent heat flow prevails, increasing cloud formation and colder temperatures. However, sensible heat flux predominates when the soil is dry (Alexander, 2011). Nonetheless, the land use type can also modulate these properties. For example, due to the forest and leaf types and thermal conductivity, Adeyeri et al. (2023b) observed positive correlations between thermal stress and most northern hemisphere primary forests. At the same time, most southern hemisphere forests have negative correlations. This suggests the potential roles of climate and land use change in modulating heatwave severity. The correlation between heatwave severity and vegetation health varies for the different basins. Fig. 3e suggests that vegetation density abates heatwave severity in most basins except Murray-Darling, Yantze, and Orange basins. This agrees with Ossola et al. (2021), who reported that vegetation reduces daytime and nighttime heat intensities. Also, vegetated areas contribute to cooling during heatwaves through evapotranspiration (Adeyeri et al., 2024; Adeyeri and Ishola, 2021; Liu et al., 2021).

Conversely, expanding bare soil and impermeable surfaces can exacerbate heat intensity (Adeyeri et al., 2017; Adeyeri et al., 2024). Nevertheless, the cooling impact of vegetation patches can be influenced by various factors, including the composition of vegetation types, their health, density, and structural characteristics (Duncan et al., 2019). The burned areas exhibit different relationships with combined moisture and thermal conditions, thermal conditions, moisture conditions, and vegetation density (Fig. 3f-i). The thermal condition positively correlates with the combined moisture and thermal effect (Fig. 3j), highlighting its critical role in the overall health of vegetation. Conversely, its relationship with moisture conditions and vegetation density is predominantly negative across many basins. Furthermore, similar to the contribution of thermal conditions to the overall vegetation health status (Fig. 3j), the moisture condition is also crucial for the overall vegetation health (Fig. 3m). Optimal combined thermal and moisture conditions enhance vegetation density (Fig. 3n).

### 3.3. Drought and vegetation stress classification

In 2002 and 2012, significant drought events occurred in various regions globally. The United States experienced a severe drought in the early 2000s, particularly intense in 2002 (Cook et al., 2007). Subsequently, the 2012 North American drought (Cook et al., 2014) caused crop failures, depleted water levels in rivers and reservoirs, and widespread wildfires. Similarly, Russia suffered a severe drought in 2012, negatively impacting wheat production and raising concerns about potential food shortages (Matsuyama et al., 2023). The Sahel region in West Africa also faced a drought that year, affecting the food and water availability for millions (Dibi-Anoh et al., 2023). Australia experienced the prolonged Millennium Drought, starting in 2002 and lasting several

years (van Dijk et al., 2013), significantly affecting agriculture and necessitating water usage restrictions in major cities. India also faced drought conditions in 2002 and 2012, leading to food security challenges and substantial agricultural losses (Bhat, 2006; Udmale et al., 2015). These events underscore the extensive impact of droughts in those years. Hence, Fig. 4 illustrates the drought and vegetation stress classification for 2002 and 2012, offering insights into the spatial distribution of these conditions during these two periods.

In 2012, a substantial portion of the Amazon, Congo, Kolyma, and Amur regions experienced extreme and exceptional drought conditions, exacerbated by unfavorable moisture conditions. In contrast, conditions were comparatively normal in 2002 (Fig. 4). The Murray-Darling basin faced exceptional drought, attributed to the Millennium drought (van Dijk et al., 2013). Unfavorable moisture conditions, rather than thermal conditions, contributed to the Brazilian drought (Cunha et al., 2015) and the Congo drought (Adeyeri et al., 2023a) in 2012. Simultaneously, the 2012 North American drought (Cook et al., 2014) and the Australian drought (van Dijk et al., 2013) resulted from a combined influence of unfavorable thermal, moisture, and moisture-thermal conditions. However, thermal conditions significantly extended the drought extent. Except for basins like the Amazon, Parana, Congo, Yukon, Volta, Murray-Darling, and Yangtze, most others experienced moderate to exceptional drought conditions in 2012. In contrast, the scenario was reversed in 2002. For example, basins like Chad and Murray-Darling, normal in 2012, faced severe and exceptional drought in 2002. The combined impact of thermal and moisture conditions resulted in varying categories, extents, and distributions of drought conditions across the basins.

Insufficient precipitation leading to unfavorable moisture conditions can contribute to drought development, while exceptionally high temperatures can create suboptimal thermal conditions, potentially exacerbating droughts. Higher temperatures intensify evapotranspiration, increasing atmospheric moisture and facilitating precipitation through moisture convergence at lower altitudes (Adeyeri et al., 2020b; Ahmed et al., 2023; Berg et al., 2009). This increases water availability due to intensified precipitation events (Adeyeri et al., 2020b). However, dry soil conditions impede moisture convergence, potentially resulting in reduced precipitation and elevated temperatures, further aggravating drought. Additionally, the interplay between moisture, temperature, and drought feedback can disrupt the water cycle and affect atmospheric circulation patterns, influencing regional precipitation patterns (Algarra et al., 2020; National Geographic). Dry conditions and changes in vegetation can alter soil hydraulic properties, potentially contributing to shifts in the link between rainfall and drought.

Furthermore, vegetation degradation and soil crusting can reduce water-holding capacity, promoting surface runoff and groundwater recharge, contributing to the '*Sahelian paradox*' observed during a prolonged drought in the Sahel (Adeyeri et al., 2020a,b; Descroix et al., 2009). Conversely, Saft et al. (2015) demonstrated that a decrease in rainfall percentage in water-limited environments could result in an increased percentage change in streamflow, disrupting moisture, temperature, and evaporation feedback mechanisms, thereby influencing drought onset and progression (Adeyeri et al., 2023a).

Also, in 2012, the Congo, Amazon, Mississippi, and Colorado basins experienced extreme and moderate vegetation stress due to moisture conditions, while other basins faced either light vegetation stress or normal/favorable conditions (Fig. 4). In contrast, the Congo and Amazon basins had favorable conditions in 2002. However, vegetation states are not necessarily favorable even in normal conditions and no drought. For instance, the Congo basin had normal conditions without drought due to thermal contributions in 2002 and 2012. However, these conditions do not yield favorable vegetation states (Fig. 4). Overall, moisture, thermal, and combined moisture and thermal conditions vary across drought and vegetation stress categories (Fig. 4). Nevertheless, drought conditions resulting from these factors led to vegetation stress.

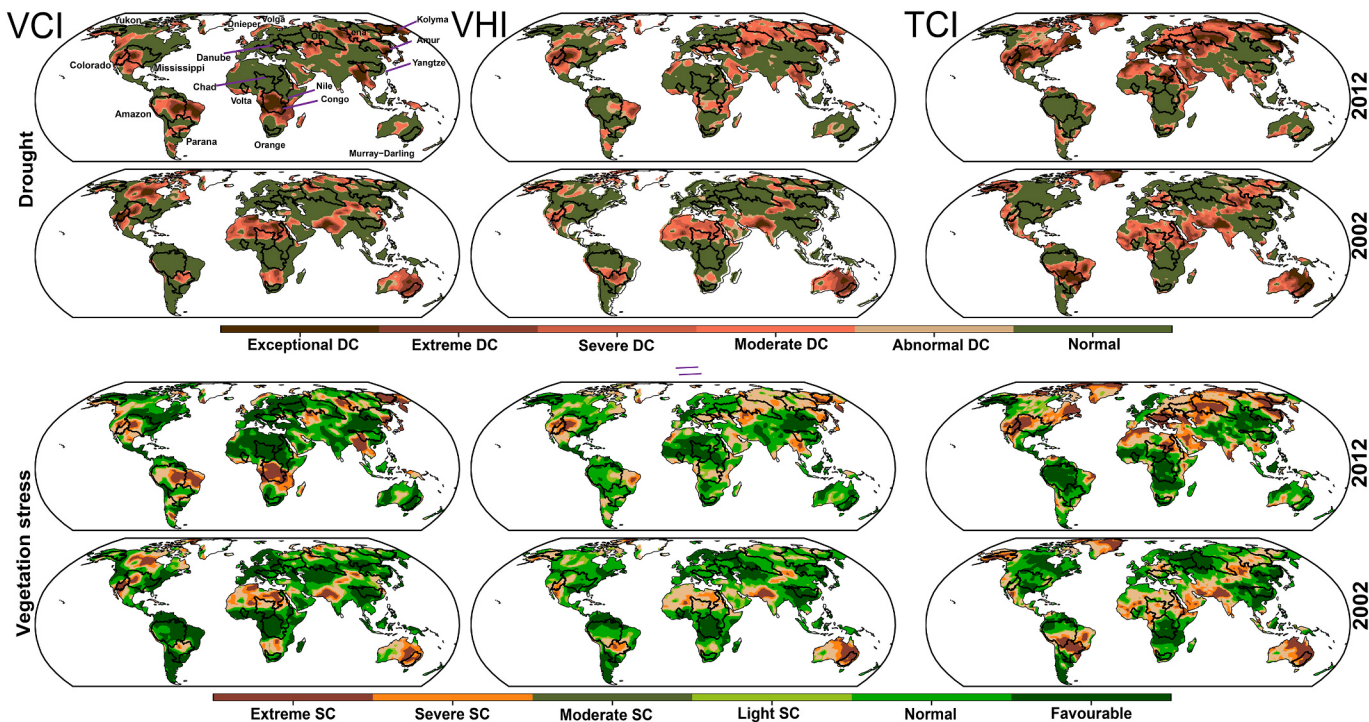


**Fig. 4.** Moisture condition (VCI), combined moisture and thermal condition (VHI), and thermal condition (TCI) contributions to drought and vegetation stress of 2002 and 2012. The black polygons represent basins.

#### 3.4. Trends in CDWVHS events

After identifying the distinctive characteristics of CDWVHS for various basins, it becomes necessary to quantify the trends. This quantification is vital for a complete comprehension of their evolution. From

1982 to 2014, most basins (excluding the Congo and Colorado) exhibit a significant positive VCI trend (Fig. 5a), indicating improved moisture conditions. However, these positive trends in most basins range from 10 % to 20 % per decade, with the Danube and Nile basins displaying the highest positive trends (>30 % per decade). The combined moisture and

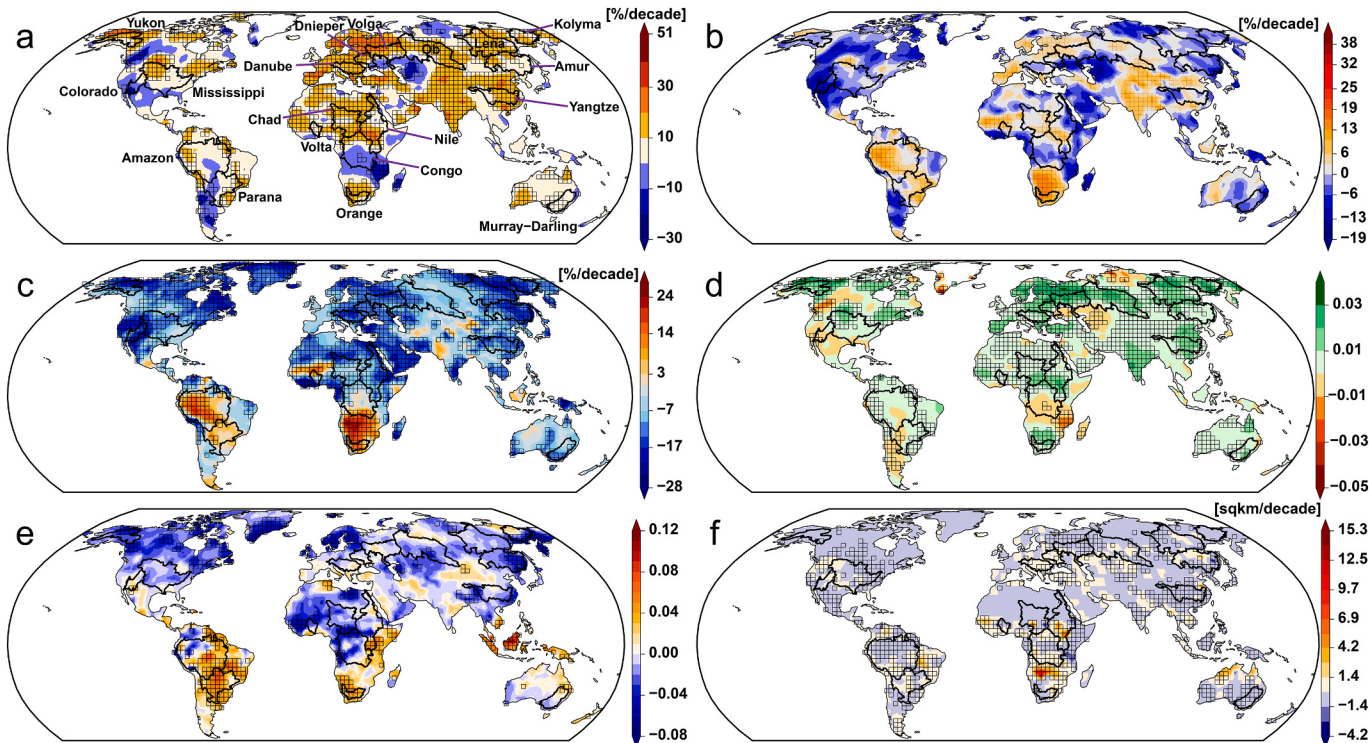


**Fig. 5.** Decadal trend for (a) VCI, (b) VHI, (c) TCI, (d) vegetation density, (e) heatwave severity, and (f) burned area. Hatchings represent significant trends at a 95 % confidence level. The black polygons represent basins.

thermal condition (Fig. 5b) presents mixed decadal trends, with the Parana, Amazon, Orange, and Murray-Darling basins primarily showing positive trends. Conversely, the thermal condition (Fig. 5c) predominantly displays negative trends, except for the Amazon and Orange basins. Furthermore, the Nile and Chad basins exhibit maximum burned area trends of up to  $10 \text{ km}^2$  per decade, indicating increased wildfire occurrences due to vegetation density and subsequent foliage drying driven by climate change and unsustainable land use practices (Adeyeri et al., 2023b; Cook et al., 2020; Yu et al., 2022).

### 3.5. Dynamic changes in CDVWHS events

Figs. 6 and S2 illustrate the dynamic changes in CDVWHS events. For example, in the Australian Millennium drought era (van Dijk et al., 2013), the Murray-Darling basin exhibits notably low VCI, VHI, and TCI values. Specifically, the driest period in 2005 and 2006 is characterized by a VCI of only 9 % (Fig. 6a), while 2001 records the most thermally adverse conditions with a TCI of 8 % (Fig. 6c). Furthermore, the least favorable VHI condition is observed in 2006, reaching 11 % (Fig. 6b). These instances highlight the compound unfavorable conditions involving moisture, thermal factors, or a combination of both during the Millennium drought era. However, it is important to note that these conditions do not correlate with the maximum burned area or the most severe heatwaves, as illustrated in Fig. S2, indicating the complex factors influencing wildfire occurrences. In contrast, the maximum burned area of  $393 \text{ km}^2$  in 1984 aligns with the most extensive fire occurrence in the western division of New South Wales. This event resulted in the loss of 40,000 livestock and four recorded fatalities (ABRC, 2010). Notably, the Murray-Darling basin witnessed the highest VCI in 2010, reaching 100 %. This peak is attributed to the prompt ending of the Australian drought due to La Niña weather conditions, which caused floods in specific areas (Forootan et al., 2019; van Dijk et al., 2013). Other basin-specific observations include the highest VHI in the Danube basin in 1996 (92 %), the highest TCI in the Dnieper basin in 1993 (100 %), the highest burned area in the Volta basin in 1996 ( $1688 \text{ km}^2$ ), and the most

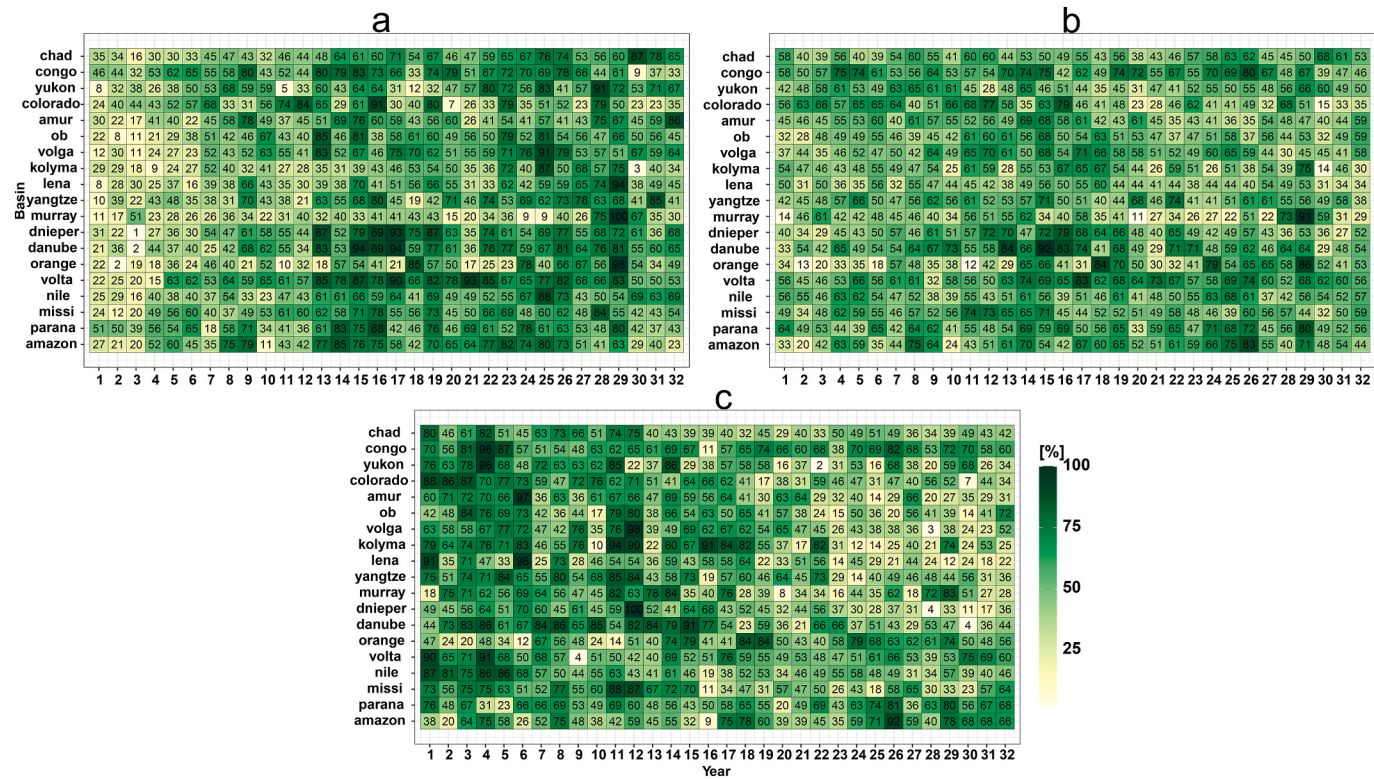
severe heatwave in the Parana basin in 2014. The variations observed across basins can also be attributed to the significant influence of oceanic climate variability patterns (Ade Resco Dios et al., 2023; Justino et al., 2023; Zhao et al., 2022).

### 3.6. A comparative analysis of CDVWHS events related to wildfires in 2012

This section investigates the anomalous vegetation-related events contributing to the 2012 wildfires that ravaged Siberia (specifically, Kolyma, Lena, and Ob basins), Australia, and North America (including the Mississippi and Colorado basins). While prior studies (e.g., Cardil et al., 2023; Huang et al., 2023; Pérez-Invernón et al., 2023) have linked wildfires to climate variability, they have not explored their relationship with anomalous vegetation events. Hence, the focus here is on vegetation attributes connected to the 2012 wildfires, where positive anomalies denote favorable conditions related to moisture (Fig. 7a), combined moisture and thermal conditions (Fig. 7b), thermal conditions (Fig. 7c), higher vegetation density (Fig. 7d), increased heatwave severity (Fig. 7e), and elevated wildfire occurrences (Fig. 7f).

In the context of the 2012 Siberian fires, particularly in the Ob basin, despite favorable moisture conditions (Fig. 7a), there are concurrent anomalous unfavorable conditions regarding both temperature and moisture (Fig. 7b) and thermal conditions (Fig. 7c). These conditions coincide with heightened heatwave severity and a larger burned area (Fig. 7f), potentially associated with a positive anomaly in vegetation density (Fig. 7d). This increased vegetation density likely provided more fuel for wildfires, consequently escalating fire carbon emissions (Yu et al., 2022).

Contrarily, the 2012 wildfires in North America are linked to negative anomalous conditions in moisture (Fig. 7a), thermal condition (Fig. 7c), and their combination (Fig. 7b). Compared to the Siberian fires, the North American fires display lower positive anomalies in burned areas (Fig. 7f) due to negative anomalous vegetation density (Fig. 7d), resulting in less available fuel for the wildfires (Jyoteeshkumar



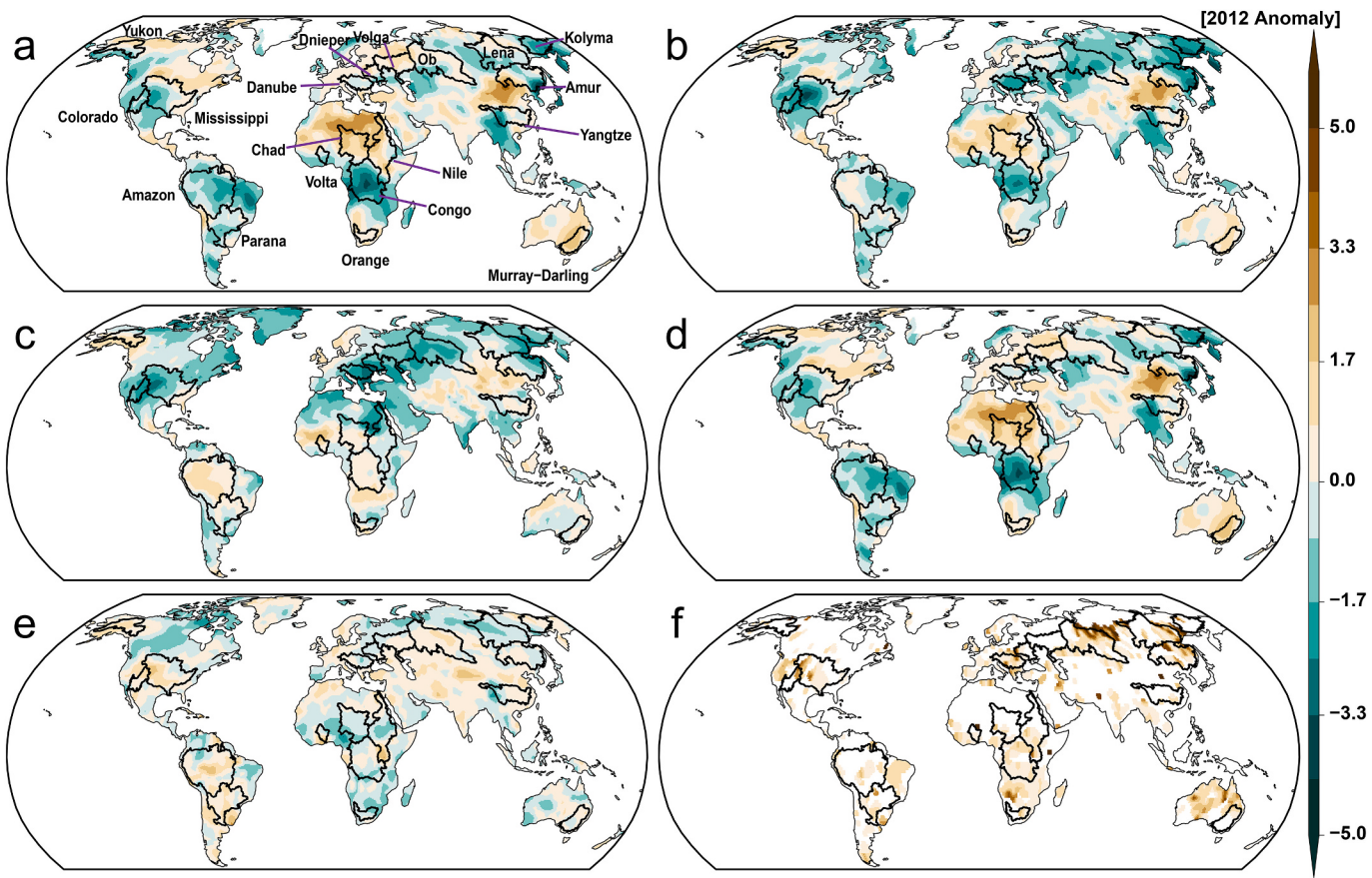


**Fig. 7.** 2012 wildfire events. Anomaly for (a) VCI, (b) VHI, (c) TCI, (d) vegetation density, (e) heatwave severity, and (f) burned area. The black polygons represent basins. Positive anomalies denote favorable conditions related to moisture (a), combined moisture and thermal conditions (b), thermal conditions (c), higher vegetation density (d), increased heatwave severity (e), and elevated wildfire occurrences (f).

(reddy et al., 2021b). Nonetheless, the heatwaves are more severe (Fig. 7e), possibly due to concurrent negative anomalous conditions in moisture, thermal aspects, and their combined contributions, highlighting the compounded nature of these events and their interplay. The 2012 Australian wildfires are associated with more negative anomalous moisture conditions and less negative anomalous thermal conditions (Fig. 7a, c). While each location experienced distinct wildfire issues, shared factors such as human activities, climate change, extreme weather conditions, and vegetation attributes play pivotal roles in igniting and spreading these fires.

### 3.7. Time-frequency relationship between climate teleconnections and CDVWHS events

The joint time-frequency variation signifies localized changes in power within a time series. The Cross Wavelet Transform (XWT) identifies regions in time and frequency space where two time series exhibit high common power. However, since both time series may not concurrently display high common power, the Wavelet Coherence (WTC) between two Continuous Wavelet Transforms (CWT) is used to detect areas on the series with significant coherence.

Fig. 8 illustrates the correlation between thermal conditions and various climate teleconnections in the Amazon basin. In Fig. 8a, the XWT analysis between TCI and TNA reveals consistent powers for most years. However, there is a negative correlation between the common powers of the two series in the 4 to 5-year band from 1988 to 1990. On the other hand, the phase angle between the 3 to 4-year band from 1995 to 1999 indicates that TCI leads the TNA signal. Additionally, the common power of the 8 to 10-year band from 1995 to 2005 indicates

that the TCI signal precedes the NAO signal (Fig. 8b). Moreover, there is a negative correlation between the common powers of TCI and DMI in the 6 to 10-year band from 1995 to 2005 (Fig. 8e). Furthermore, negative correlations exist between similar common powers in the relationship between TCI and NINO (Fig. 8f), particularly in the 3 to 6-year bands from 1982 to 2006. The wavelet coherence plot between TNA and TCI series (Fig. 8g) shows a dependency between 0.5 and 1 in most bands during the study period. On the other hand, NAO demonstrates a lower dependency (Fig. 8f). NP exhibits mostly low dependencies (<0.4) with TCI series in the 3 to 6-year band between 2003 and 2014. PNA mostly shows <0.8, while DMI displays high positive dependencies (>0.8) in the 2 to 3-year band between 1985 and 2014. However, the DMI series lags behind the TCI series (Fig. 8k). Additionally, there are high dependencies (>0.8) between NINO and TCI. However, the NINO series mostly lags the TCI series (Fig. 8l). These findings indicate that various climate teleconnections have diverse effects on the TCI of the Amazon basin. Notably, the NINO signals have the most significant impact on the TCI signals of the Amazon basin. While some bands show common powers between NINO and burned area in the Amazon (Fig. S5f), the dependency is generally low, except for the 5 to 6-year band (Fig. S5l). In contrast to the findings of Justino et al. (2023), who suggest that the El Niño-Southern Oscillation weakens fire activity in Equatorial Africa, our study emphasizes a strong relationship between NINO and burned areas, particularly in the Congo basin. This discrepancy may be attributed to the different study periods examined in the respective studies. Nevertheless, a warmer tropical North Atlantic has been linked to increasing wildfires in the Amazon and Africa (Justino et al., 2023).

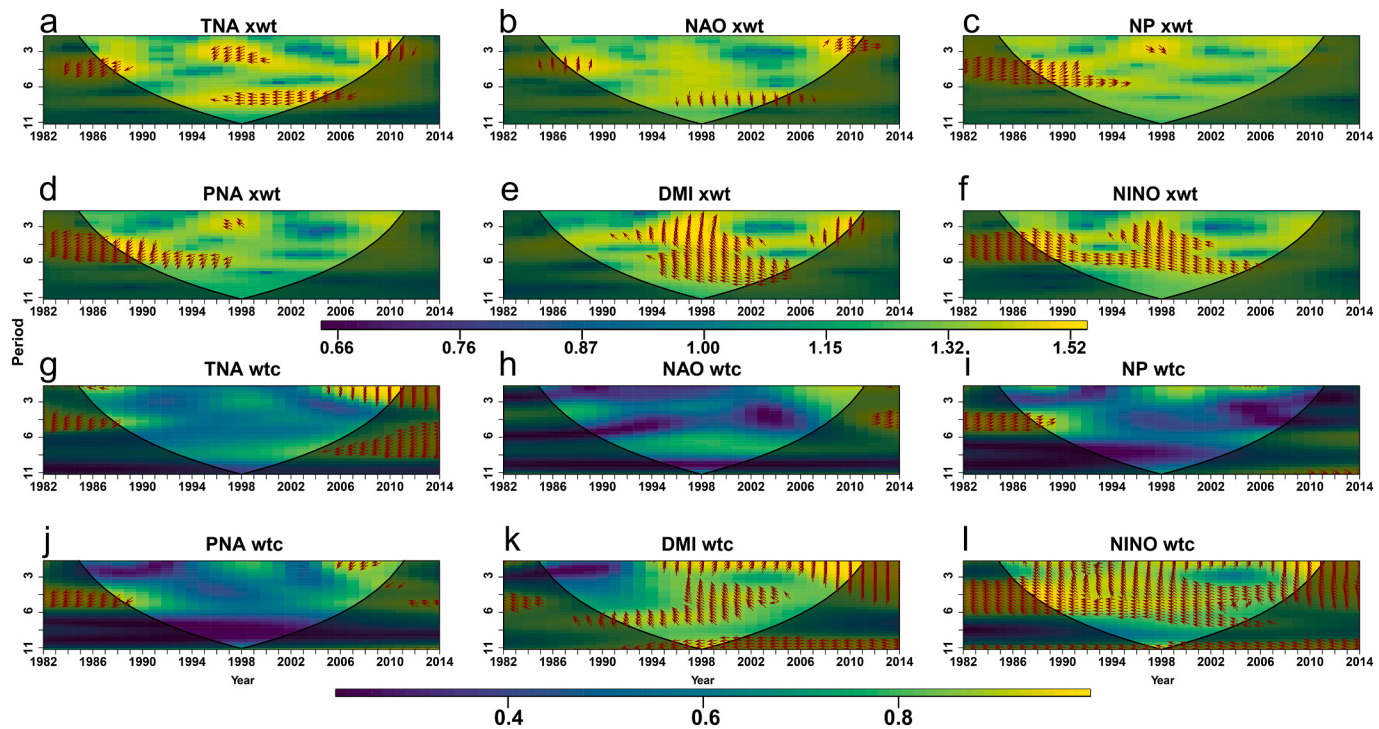


**Fig. 8.** Cross wavelet transform (a-f) and wavelet coherence (g-l) between atmospheric teleconnections and TCI during the extended summer of 1982–2014 in the Amazon basin. The teleconnections are the Pacific/North American teleconnection pattern (PNA), Tropical Northern Atlantic Index (TNA), North Atlantic Oscillation (NAO), North Pacific Index (NP), Dipole Mode Index (DMI), and Niño 3.4 SST Index (NINO). Warmer colors indicate strong connections (coherence), while cooler colors represent less dependency between series. The arrow denotes the lead/lag phase relationships of the analyzed series. A zero-phase difference signifies that the two time series move together on a given scale. When the two series are in phase (arrows pointing to the right), the variables move in the same direction, indicating positive correlations. Conversely, for an anti-phase signal (arrows pointing to the left), the variables move in opposite directions, suggesting a negative relationship between them (Adeyeri and Ishola, 2021). Arrows pointing to the right-up or left-down suggest that the first variable is leading by 90°, while arrows pointing to the right-down or left-up indicate that the first variable is lagging.

Supplementary Figs. S3 and S4 illustrate the climate teleconnection relationships with VCI and VHI in the Amazon, respectively. In summary, analyzing the teleconnection and VHIs signals reveals a combined impact of both moisture and thermal conditions on cumulative vegetation response (Kogan et al., 2011). This approach enables more precise identification of affected areas and periods than relying solely on weather-based features like precipitation and temperature (Jiang et al., 2021; Justino et al., 2023). Moreover, we do not observe consistent patterns of power coherence between climate teleconnections and heatwave severity (Fig. S6). Nevertheless, some level of coherence in the signal patterns is evident. We identify notable strong positive correlations ( $>0.8$ ) in specific frequency bands. For instance, a high correlation is found in the 3 to 4-year band between 1995 and 2002, involving TNA and heatwave severity; in the 1 to 3-year band between 2006 and 2010, associating NAO with heatwave severity; and in the 4 to 6-year band between 1982 and 1994, linking NP with heatwave severity. Supplementary Figs. S5 through S18 present XWT and wavelet coherence analyses of climate teleconnections in relation to other CDVWHS events in various basins.

### 3.8. Projected climate change signal in heatwave severity

Climate models are instrumental in studying climate change, projecting future climate conditions, assessing potential impacts on ecosystems and societies, and formulating climate adaptation and mitigation strategies. However, before considering future climate change scenarios, it is crucial to quantify the agreement between climate models and the reference data during the historical period (Adeyeri et al., 2019). Using ten CMIP6 multi-model ensemble mean (Table S2),

Fig. S19a reveals different levels of biases between the multi-model ensemble mean and the reference data. The discrepancies can be ascribed to various factors, including differences in land surface schemes and modeling characteristics like solar radiation, vegetation, and cloud features or other synoptic-scale system interactions (Adeyeri et al., 2022b; Grose et al., 2019; Wild et al., 2005). Additionally, Fig. S19b illustrates significant positive correlations between the multi-model ensemble mean and the reference. Therefore, there is a level of trust in the future projection.

Fig. S20a shows that most American and African basins will experience more severe heatwaves in the near future under SSP 245. However, the Yangtze and Lena basins will witness less severe heatwaves than the historical period under this scenario. This pattern is expected to recur in the far future under SSP 245 (Fig. S20b) but with varying magnitudes. In the near future, under SSP 585, there will be a general reduction in heatwave severity in most basins compared to the historical period, except for the Amazon, Congo, and Parana basins, which will experience more severe heatwaves (Fig. S20c). These findings indicate that heatwave dynamics will differ among basins in the future, likely due to the dynamics of different atmospheric phenomena (e.g., anticyclonic circulation, vertically integrated moisture flux, wind systems) and the carbon-socioeconomic scenarios, thus affecting overall drought and vegetation stress conditions (Ade Resco Dios et al., 2023; Adeyeri et al., 2023a; Adeyeri et al., 2024; Ndehedehe et al., 2023b; Peñuelas et al., 2017; Zhao et al., 2022). Furthermore, the CCS between SSP 585 far future and historical period shows that all tropical basins, Mississippi and Colorado basins, will witness more severe heatwaves under this CCS spectrum than the historical period (Fig. S20d). The comparison between SSP 245 far and near future (Fig. S20e) yields mixed CCS results.

Heatwaves are projected to be more severe in SSP 585 far future than in the near future (Fig. S20f). While previous studies have established that heatwaves are expected to become more severe in the future (Adeyeri et al., 2019; Adeyeri et al., 2022b; Adeyeri et al., 2023a; Jyoteeshkumar reddy et al., 2021a; Jyoteeshkumar reddy et al., 2021b; Perkins-Kirkpatrick and Lewis, 2020), our study utilize a broader range of the CCS spectrum to provide a more robust interpretation of heatwave severity across different future time frames. We anticipate that extreme events will be even more severe in the future, with the most significant increase in heatwave severity occurring between the near and far future under SSP 585. Various factors, such as greenhouse gas emissions, climate sensitivity, and natural variability, play crucial roles in determining the projected severity of heatwaves. While some studies suggest that specific locations may experience more frequent and intense heatwaves due to global warming (Adeyeri et al., 2019; Adeyeri et al., 2022b; Perkins et al., 2015; Perkins-Kirkpatrick and Lewis, 2020), others (e.g., Dai, 2013; Fischer et al., 2007; Miralles et al., 2014; Trenberth et al., 2014) argue that certain regions may see more frequent and severe precipitation, which could alleviate the consequences of excessive heat. Specifically, atmospheric moisture may cause evaporative cooling, reducing surface temperatures and heat stress (Trenberth et al., 2014). This process is most beneficial in places with high soil moisture content and relative humidity, as evaporation may occur more rapidly (Dai, 2013). Moreover, precipitation events increase soil moisture content, which affects the severity of heatwaves. When soil moisture is high, more solar energy is used for evapotranspiration instead of sensible heating, resulting in a surface cooling effect (Fischer et al., 2007). Additionally, moist soil can enhance atmospheric moisture transfer and the likelihood of convective precipitation, leading to additional cooling (Miralles et al., 2014). However, increased moisture availability could raise temperatures and exacerbate heatwave severity (Evan et al., 2015). Ultimately, the future trajectory of heatwave severity will depend on a complex interplay of various factors (e.g., precipitation, greenhouse gas emission, and moisture transport), making it essential to subject heatwave severity projections to a broad range of plausible scenarios to facilitate risk management.

### 3.9. Limitations and uncertainties of models

Climate models are powerful tools for understanding the climate system and projecting future changes. However, they are not without limitations and uncertainties. These stem from the intricate nature of the climate system (Reichstein et al., 2013), initial and boundary model conditions, and the unpredictable nature of future emissions (van Vuuren et al., 2011). Climate models rely on observational data for calibration and validation, which can propagate uncertainties from observation into climate models (Adeyeri et al., 2022a), especially in regions with sparse data, like polar regions and deep oceans (Rayner, 2003). Furthermore, uncertainties arise from model approximations and computational limitations in representing specific aspects of the climate system (Adeyeri et al., 2022b). Predicting future climate change involves considering various socioeconomic and emission scenarios, including technological developments, carbon emissions, economic growth, and policy decisions (O'Neill et al., 2016; van Vuuren et al., 2011). Improving the accuracy of climate models to depict the reality and non-linearity of climate systems, especially those resulting from human-induced environmental changes, will continue to be an essential aspect of future research in climate science.

However, multi-model ensembles generate simulations with consistent forcing across multiple models to quantify epistemic uncertainties (Adeyeri et al., 2020c). Using the ensemble of output from multiple models helps to cushion the effects of uncertainties associated with individual models that may not fully capture the complexities of reality (Adeyeri et al., 2020c). Nonetheless, climate models remain the most reliable means for projecting changes in future climate and possible extreme events (e.g., heatwaves, wildfire, drought, and floods)

associated with such changes, providing crucial insights for informed policy decisions. Integrating reliable observational datasets for model calibration and validation, e.g., (Adeyeri et al., 2019; Adeyeri et al., 2022a) and incorporating a broad range of plausible future scenarios into climate projections, is essential to enhance their reliability. Arguably, this should ensure more accurate projections that underpin informed climate-related decisions. Additionally, bias-correcting climate models remove historical biases relative to observation (Adeyeri et al., 2019; Adeyeri et al., 2020c; Adeyeri et al., 2023a). This correction effectively minimizes discrepancies between observed and simulated climate variables, thus reducing uncertainties present in the uncorrected climate models (Adeyeri et al., 2020c; Adeyeri et al., 2023b).

### 3.10. Implications of concurrent drought, vegetation stress, wildfires, and heatwave severity events

Compound drought, vegetation stress, wildfires, and severe heatwaves can have significant societal implications, especially in regions heavily reliant on agriculture and natural resources for sustenance. For instance, high VHIs (Fig. 2a–c) indicate healthy plants and the likelihood of a successful harvest. On the other hand, low VHIs (Fig. 4) indicate stressed plants that may be at risk of failure, leading to reduced agricultural yields and potential food shortages. Utilizing VHIs can aid in predicting crop yields and making informed agricultural management decisions (Kogan et al., 2012; Pei et al., 2018) and serve as an early warning tool for drought (Fig. 4) and food insecurity. By monitoring VHIs levels throughout the growing season, farmers can enhance their decision-making regarding irrigation, fertilizer application, and other management practices to optimize crop output. On the other hand, crop failure, lower yields, and unhealthy vegetation due to drought and vegetation stress can lead to food shortages and higher food prices. Such outcomes may disproportionately affect vulnerable populations, including rural areas and low-income households.

Heatwave severity (Jyoteeshkumar reddy et al., 2021a; Perkins and Alexander, 2013) and wildfires (Parente et al., 2019; Pérez-Invernón et al., 2023) can pose significant health risks and enhance thermal stress (Adeyeri et al., 2023b; Wondmagegn et al., 2021). Notably, more fuels are available to drive wildfires (Fig. 2f) in areas with high vegetation density (Fig. 2e), especially if the vegetation is faced with unfavorable thermal, moisture, or a combination of both conditions, and contributing further to climate change (Yu et al., 2022).

Wildfires have numerous adverse effects on ecosystems, including deforestation, biodiversity loss, and soil erosion. These repercussions are further compounded by concurrent drought, unfavorable weather patterns, and vegetation stress, resulting in long-term implications for the ecosystem (Aderián et al., 2021). Moreover, the severity of heatwaves can contribute to the spread of wildfires (Fig. 3a), as dead fine fuel becomes dry and its moisture content decreases (Jyoteeshkumar reddy et al., 2021b). Additionally, unfavorable thermal conditions can potentially exacerbate the severity of heatwaves (Fig. 3b). In the face of climate change, characterized by more frequent and intense weather events, VHIs could be invaluable in providing crucial insights into the resilience of vegetation against the stressors imposed by climate change. This, in turn, will facilitate the formulation of effective policies and management strategies aimed at mitigating the impact of climate change on biomes and, consequently, human livelihoods.

## 4. Conclusion

Extreme events like drought, vegetation stress, wildfires, and heatwave severity can wreak havoc on ecosystems, societies, and economies. These events can intersect, leading to interconnected challenges. This study explores the relationships between vegetation moisture, thermal conditions, and climate teleconnections and their impact on drought, wildfires, vegetation stress, and heatwave severity. Our findings show

regional variations in compound drought, vegetation stress, wildfires, and heatwave severity attributes. Moisture scarcity, suboptimal thermal conditions, and reduced vegetation health marginally influenced vegetation density but significantly intensified heatwave severity. Regions with dense vegetation provide more fuel for wildfires, particularly in tropical areas where climate change accelerates drying. Heatwave severity plays a crucial role in wildfire spread, driven by the dryness or low moisture content of dead fine fuel. For instance, the Siberian fires show higher positive anomalies in burned areas than North American fires, primarily due to differences in vegetation density and subsequent fuel availability.

Unfavorable thermal conditions aggravate heatwave severity, while favorable moisture conditions mitigate it. We emphasize that the contributions of moisture, thermal, and combined moisture and thermal conditions vary across the drought and vegetation stress categories. Regardless of the specific factors, drought conditions lead to vegetation stress, but these trends vary across basins due to contrasting local-scale vegetation dynamics and land use practices. Furthermore, the variability in climate teleconnection associated with compound drought, vegetation stress, wildfires, and heatwave severity varies for different basins. We highlight both the primary modes of variability and how those modes evolve. Future extreme occurrences are likely to be more severe, with the most significant changes in heatwave severity magnitude occurring between the near and far future under SSP 585. Nevertheless, the future trajectory of heatwave severity is influenced by multiple factors, emphasizing the importance of considering a wide range of plausible scenarios for risk management and projections.

Overall, the combined occurrence of drought, vegetation stress, wildfires, and the severity of heatwaves can have significant societal consequences, including food shortages, economic costs, health concerns, and environmental degradation. Therefore, implementing appropriate policies and management methods to mitigate these effects and maintain ecosystem and livelihood resilience is essential. Proactive actions such as investing in research and development of novel solutions, supporting sustainable land use practices, and employing adaptive management techniques can increase resilience in impacted regions and promote sustainable development.

#### CRediT authorship contribution statement

**Oluwafemi E. Adeyeri:** Writing – review & editing, Writing – original draft, Visualization, Validation, Software, Resources, Methodology, Investigation, Formal analysis, Data curation, Conceptualization. **Wen Zhou:** Validation, Supervision, Resources, Project administration, Funding acquisition. **Christopher E. Ndehedehe:** Writing – review & editing, Validation. **Xuan Wang:** Supervision.

#### Declaration of competing interest

The authors declare that they have no known competing financial interests or personal relationships that could have appeared to influence the work reported in this paper.

#### Data availability

CMIP6 data are publicly available through the Earth System Grid Federation at <http://esgf.llnl.gov/>.

The NDVI data is available through Pinzon (Pinzon and Tucker, 2014) at <https://data.tpdc.ac.cn/en/data/9775f2b4-7370-4e5e-a537-3482c9a83d88/>.

The brightness temperature dataset is available through Kobayashi (Kobayashi et al., 2015) at <http://rda.ucar.edu/datasets/ds628.1/>.

Heatwave was calculated using an open-source platform, “CDO” (Schulzweida, 2022).

#### Acknowledgments

This work is supported by the National Natural Science Foundation of China Grants (42288101, 42120104001, 42192563) and Hong Kong RGC General Research Fund 11300920. Christopher E. Ndehedehe is supported by the Australian Research Council grant (DE230101327). We thank the World Climate Research Programme for coordinating and promoting CMIP6 through its Working Group on Coupled Modeling. We appreciate the different climate modeling groups for developing and making their simulations available. We acknowledge the Earth System Grid Federation for storing and giving access to records. We acknowledge Hyo-Jeong Kim of the School of Energy and Environment at the City University of Hong Kong for the insightful discussions regarding wildfires.

#### Appendix A. Supplementary data

Supplementary data to this article can be found online at <https://doi.org/10.1016/j.scitotenv.2023.169261>.

#### References

- Abdulla-Al, K., Bakshi, A., Saha, M., Faisal, A.A., Almulhim, A.I., Rahaman, Z.A., et al., 2023. Assessment and prediction of index based agricultural drought vulnerability using machine learning algorithms. *Sci. Total Environ.* 867, 161394 <https://doi.org/10.1016/j.scitotenv.2023.161394>.
- Aboka, A., Mishra, V., 2015. Prediction of vegetation anomalies to improve food security and water management in India. *Geophys. Res. Lett.* 42 (13), 5290–5298. <https://doi.org/10.1002/2015GL063991>.
- Abofazl, R., Gurdak, J.J., 2020. Large-scale climate variability controls on climate, vegetation coverage, lake and groundwater storage in the Lake Urmia watershed using SSA and wavelet analysis. *Sci. Total Environ.* 724, 138273 <https://doi.org/10.1016/j.scitotenv.2020.138273>.
- ABRC, 2010. Final Report. *Parliament of Victoria, 2009 Victorian Bushfires Royal Commission, [Melbourne]*.
- Adesco Dios, V., Cunill Camprubí, À., He, Y., Han, Y., Yao, Y., 2023. North-south anti-phase of wildfire activity across the pyroregions of continental China driven by NAO and the Antarctic oscillation. *Sci. Total Environ.* 859 (Pt 2), 160386 <https://doi.org/10.1016/j.scitotenv.2022.160386>.
- Aderián, C., Rodrigues, M., Ramirez, J., de-Miguel, S., Silva, C.A., Mariani, M., et al., 2021. Coupled effects of climate teleconnections on drought, Santa Ana winds and wildfires in southern California. *Sci. Total Environ.* 765, 142788 <https://doi.org/10.1016/j.scitotenv.2020.142788>.
- Adeyeri, O.E., Ishola, K.A., 2021. Variability and trends of actual evapotranspiration over West Africa: the role of environmental drivers. *Agric. For. Meteorol.* 308–309, 108574 <https://doi.org/10.1016/j.agrformet.2021.108574>.
- Adeyeri, O.E., Akinsanola, A.A., Ishola, K.A., 2017. Investigating surface urban heat island characteristics over Abuja, Nigeria: relationship between land surface temperature and multiple vegetation indices. *Remote Sens. Appl. Soc. Environ.* 7, 57–68. <https://doi.org/10.1016/j.rsase.2017.06.005>.
- Adeyeri, O.E., Lawin, A.E., Laux, P., Ishola, K.A., Ige, S.O., 2019. Analysis of climate extreme indices over the Komadugu-Yobe basin, Lake Chad region: past and future occurrences. *Weather Clim. Extr.* 23, 100194 <https://doi.org/10.1016/j.wace.2019.100194>.
- Adeyeri, O.E., Laux, P., Arnault, J., Lawin, A.E., Kunstmann, H., 2020a. Conceptual hydrological model calibration using multi-objective optimization techniques over the transboundary Komadugu-Yobe basin, Lake Chad Area, West Africa. *J. Hydrol. Reg. Stud.* 27, 100655 <https://doi.org/10.1016/j.ejrh.2019.100655>.
- Adeyeri, O.E., Laux, P., Lawin, A.E., Ige, S.O., Kunstmann, H., 2020b. Analysis of hydrometeorological variables over the transboundary Komadugu-Yobe basin, West Africa. *J. Water Clim. Chang.* 11 (4), 1339–1354. <https://doi.org/10.2166/wcc.2019.283>.
- Adeyeri, O.E., Laux, P., Lawin, A.E., Oyekan, K.S.A., 2020c. Multiple bias-correction of dynamically downscaled CMIP5 climate models temperature projection: a case study of the transboundary Komadugu-Yobe river basin, Lake Chad region, West Africa. *SN Appl. Sci.* 2 (7) <https://doi.org/10.1007/s42452-020-3009-4>.
- Adeyeri, O.E., Laux, P., Ishola, K.A., Zhou, W., Balogun, I.A., Adeyewa, Z.D., et al., 2022a. Homogenizing meteorological variables: impact on trends and associated climate indices. *J. Hydrol.* 607, 127585 <https://doi.org/10.1016/j.jhydrol.2022.127585>.
- Adeyeri, O.E., Zhou, W., Wang, X., Zhang, R., Laux, P., Ishola, K.A., et al., 2022b. The trend and spatial spread of multisectoral climate extremes in CMIP6 models. *Sci. Rep.* 12 (1), 21000 <https://doi.org/10.1038/s41598-022-25265-4>.
- Adeyeri, O.E., Zhou, W., Laux, P., Ndehedehe, C.E., Wang, X., Usman, M., et al., 2023a. Multivariate drought monitoring, propagation, and projection using bias-corrected general circulation models. *Earth's Future* 11 (4). <https://doi.org/10.1029/2022EF003303>.

- Adeyeri, O.E., Zhou, W., Laux, P., Wang, X., Dieng, D., Widana, L.A., et al., 2023b. Land use and land cover dynamics: implications for thermal stress and energy demands. *Renew. Sust. Energ. Rev.* 179, 113274 <https://doi.org/10.1016/j.rser.2023.113274>.
- Adeyeri, O.E., Folorunsho, A.H., Ayegbusi, K.I., Bobde, V., Adeliyi, T.E., Ndehedehe, C. E., et al., 2024. Land surface dynamics and meteorological forcings modulate land surface temperature characteristics. *Sustain. Cities Soc.* 101, 105072 <https://doi.org/10.1016/j.scs.2023.105072>.
- AghaKouchak, A., Cheng, L., Mazdiyasni, O., Farahmand, A., 2014. Global warming and changes in risk of concurrent climate extremes: insights from the 2014 California drought. *Geophys. Res. Lett.* 41 (24), 8847–8852. <https://doi.org/10.1002/2014GL062308>.
- Ahmed, N., Lü, H., Ahmed, S., Adeyeri, O.E., Ali, S., Hussain, R., et al., 2023. Transboundary river water availability to Ravi Riverfront under changing climate: a step towards sustainable development. *Sustainability* 15 (4), 3526. <https://doi.org/10.3390/su15043526>.
- Alexander, L., 2011. Extreme heat rooted in dry soils. *Nat. Geosci.* 4 (1), 12–13. <https://doi.org/10.1038/ngeo1045>.
- Algarra, I., Nieto, R., Ramos, A.M., Eiras-Barca, J., Trigo, R.M., Gimeno, L., 2020. Significant increase of global anomalous moisture uptake feeding landfalling atmospheric rivers. *Nat. Commun.* 11 (1), 5082. <https://doi.org/10.1038/s41467-020-18876-w>.
- Allen, C.D., Macalady, A.K., Chenchouni, H., Bachelet, D., McDowell, N., Vennettier, M., et al., 2010. A global overview of drought and heat-induced tree mortality reveals emerging climate change risks for forests. *For. Ecol. Manag.* 259 (4), 660–684. <https://doi.org/10.1016/j.foreco.2009.09.001>.
- Allen, M.A., Roberts, D.A., McFadden, J.P., 2021. Reduced urban green cover and daytime cooling capacity during the 2012–2016 California drought. *Urban Clim.* 36, 100768 <https://doi.org/10.1016/j.uclim.2020.100768>.
- Ault, T.R., 2020. On the essentials of drought in a changing climate. *Science* (New York, N.Y.) 368 (6488), 256–260. <https://doi.org/10.1126/science.aaz5492>.
- Ballarin, A.S., Barros, G.L., Cabrera, M.C., Wendland, E.C., 2021. A copula-based drought assessment framework considering global simulation models. *J. Hydrol. Reg. Stud.* 38, 100970 <https://doi.org/10.1016/j.ejrh.2021.100970>.
- Bento, V., Trigo, I., Gouveia, C., DaCamara, C., 2018. Contribution of land surface temperature (TCI) to vegetation health index: a comparative study using clear sky and all-weather climate data records. *Remote Sens.* 10 (9), 1324. <https://doi.org/10.3390/rs10091324>.
- Berg, P., Haerter, J.O., Thejll, P., Piani, C., Hagemann, S., Christensen, J.H., 2009. Seasonal characteristics of the relationship between daily precipitation intensity and surface temperature. *J. Geophys. Res.* 114 (D18) <https://doi.org/10.1029/2009JD012008>.
- Bhat, G.S., 2006. The Indian drought of 2002—a sub-seasonal phenomenon? *Q. J. R. Meteorol. Soc.* 132 (621), 2583–2602. <https://doi.org/10.1256/qj.05.13>.
- Bokushsheva, R., Kogan, F., Vitkovskaya, I., Conradt, S., Batyrbayeva, M., 2016. Satellite-based vegetation health indices as a criteria for insuring against drought-related yield losses. *Agric. For. Meteorol.* 220, 200–206. <https://doi.org/10.1016/j.agrformet.2015.12.066>.
- Cardil, A., Rodrigues, M., Tapia, M., Barbero, R., Ramírez, J., Stoof, C.R., et al., 2023. Climate teleconnections modulate global burned area. *Nat. Commun.* 14 (1), 427 <https://www.nature.com/articles/s41467-023-36052-8>.
- Chaves, M.M., Maroco, J.P., Pereira, J.S., 2003. Understanding plant responses to drought - from genes to the whole plant. *Funct. Plant Biol.* 30 (3), 239–264. <https://doi.org/10.1071/FP02076>.
- Cheng, Y., Zhang, K., Chao, L., Shi, W., Feng, J., Li, Y., 2023. A comprehensive drought index based on remote sensing data and nested copulas for monitoring meteorological and agroecological droughts: a case study on the Qinghai-Tibet Plateau. *Environ. Model Softw.* 161, 105629 <https://doi.org/10.1016/j.envsoft.2023.105629>.
- Chuvieco, E., Pettinari, M.L., Otón, G., 2020. *ESA Fire Climate Change Initiative (Fire\_cci): AVHRR-LTDR Burned Area Grid Product, Version 1.1*.
- Cook, B.I., Smerdon, J.E., Seager, R., Cook, E.R., 2014. Pan-continental droughts in North America over the last millennium\*. *J. Clim.* 27 (1), 383–397. <https://doi.org/10.1175/JCLI-D-13-00100.1>.
- Cook, B.I., Mankin, J.S., Marvel, K., Williams, A.P., Smerdon, J.E., Anchukaitis, K.J., 2020. Twenty-first century drought projections in the CMIP6 forcing scenarios. *Earth's Future* 8 (6), e2019EF001461. <https://doi.org/10.1029/2019EF001461>.
- Cook, E.R., Seager, R., Cane, M.A., Stahle, D.W., 2007. North American drought reconstructions, causes, and consequences. *Earth Sci. Rev.* 81 (1–2), 93–134. <https://doi.org/10.1016/j.earscirev.2006.12.002>.
- Cunha, A., Alvalá, R.C., Nobre, C.A., Carvalho, M.A., 2015. Monitoring vegetative drought dynamics in the Brazilian semi-arid region. *Agric. For. Meteorol.* 214–215, 494–505. <https://doi.org/10.1016/j.agrformet.2015.09.010>.
- Dai, A., 2011. Drought under global warming: a review. *WIREs Clim. Change* 2 (1), 45–65. <https://doi.org/10.1002/wcc.81>.
- Dai, A., 2013. Increasing drought under global warming in observations and models. *Nat. Clim. Chang.* 3 (1), 52–58. <https://doi.org/10.1038/nclimate1633>.
- Derradj, T., Belksier, M.-S., Bouznad, I.-E., Zebsa, R., Bengusmia, D., Guastaldi, E., 2023. Spatio-temporal drought monitoring and detection of the areas most vulnerable to drought risk in Mediterranean region, based on remote sensing data (Northeastern Algeria). *Arab. J. Geosci.* 16 (1) <https://doi.org/10.1007/s12517-022-11060-y>.
- Descroix, L., Mahé, G., Lebel, T., Favreau, G., Galle, S., Gautier, E., et al., 2009. Spatio-temporal variability of hydrological regimes around the boundaries between Sahelian and Sudanian areas of West Africa: a synthesis. *J. Hydrol.* 375 (1–2), 90–102. <https://doi.org/10.1016/j.jhydrol.2008.12.012>.
- Dibi-Anoh, P.A., Koné, M., Gerdener, H., Kusche, J., N'Da, C.K., 2023. Hydrometeorological extreme events in West Africa: droughts. *Surv. Geophys.* 44 (1), 173–195. <https://doi.org/10.1007/s10712-022-09748-7>.
- Diffenbaugh, N.S., Ashfaq, M., 2010. Intensification of hot extremes in the United States. *Geophys. Res. Lett.* 37 (15) <https://doi.org/10.1029/2010GL043888> (n/a-n/a).
- Dole, R., Hoerling, M., Perlitz, J., Eischeid, J., Pegion, P., Zhang, T., et al., 2011. Was there a basis for anticipating the 2010 Russian heat wave? *Geophys. Res. Lett.* 38 (6) <https://doi.org/10.1029/2010GL046582> (n/a-n/a).
- Drumond, A., Gimeno, L., Nieto, R., Trigo, R.M., Vicente-Serrano, S.M., 2017. Drought episodes in the climatological sinks of the Mediterranean moisture source: the role of moisture transport. *Glob. Planet. Chang.* 151, 4–14. <https://doi.org/10.1016/j.gloplacha.2016.12.004>.
- Duncan, J.M.A., Boruff, B., Saunders, A., Sun, Q., Hurley, J., Amati, M., 2019. Turning down the heat: an enhanced understanding of the relationship between urban vegetation and surface temperature at the city scale. *Sci. Total Environ.* 656, 118–128. <https://doi.org/10.1016/j.scitotenv.2018.11.223>.
- Erasmi, S., Schucknecht, A., Barbosa, M., Matschullat, J., 2014. Vegetation greenness in northeastern Brazil and its relation to ENSO warm events. *Remote Sens.* 6 (4), 3041–3058. <https://doi.org/10.3390/rs6043041>.
- Evan, A.T., Flamant, C., Lavayse, C., Kocha, C., Saci, A., 2015. Water vapor-forced greenhouse warming over the Sahara Desert and the recent recovery from the Sahelian drought. *J. Clim.* 28 (1), 108–123. <https://doi.org/10.1175/JCLI-D-14-0039.1>.
- Farooq, M., Wahid, A., Kobayashi, N., Fujita, D., Basra, S.M.A., 2009. Plant drought stress: effects, mechanisms and management. *Agron. Sustain. Dev.* 29 (1), 185–212. <https://doi.org/10.1051/agro:2008021>.
- Fischer, E.M., Seneviratne, S.I., Vidale, P.L., Lüthi, D., Schär, C., 2007. Soil moisture-atmosphere interactions during the 2003 European Summer Heat Wave. *J. Clim.* 20 (20), 5081–5099. <https://doi.org/10.1175/JCLI4288.1>.
- Forootan, E., Khaki, M., Schumacher, M., Wulfmeyer, V., Mehrmegar, N., van Dijk, A.I.J. M., et al., 2019. Understanding the global hydrological droughts of 2003–2016 and their relationships with teleconnections. *Sci. Total Environ.* 650 (Pt 2), 2587–2604. <https://doi.org/10.1016/j.scitotenv.2018.09.231>.
- Grose, M.R., Foster, S., Risbey, J.S., Osbrrough, S., Wilson, L., 2019. Using indices of atmospheric circulation to refine southern Australian winter rainfall climate projections. *Clim. Dyn.* 53 (9–10), 5481–5493. <https://doi.org/10.1007/s00382-019-04880-4>.
- Hao, Z., AghaKouchak, A., 2013. Multivariate standardized drought index: a parametric multi-index model. *Adv. Water Resour.* 57, 12–18. <https://doi.org/10.1016/j.advwatres.2013.03.009>.
- Huang, X., Ding, K., Liu, J., Wang, Z., Tang, R., Xue, L., et al., 2023. Smoke-weather interaction affects extreme wildfires in diverse coastal regions. *Science* (New York, N.Y.) 379 (6631), 457–461. <https://doi.org/10.1126/science.add9843>.
- Jiang, R., Liang, J., Zhao, Y., Wang, H., Xie, J., Lu, X., et al., 2021. Assessment of vegetation growth and drought conditions using satellite-based vegetation health indices in Jing-Jin-Ji region of China. *Sci. Rep.* 11 (1), 13775 <https://doi.org/10.1038/s41598-021-93328-z>.
- Justino, F., Bromwich, D.H., Wang, S.-H., Althoff, D., Schumacher, V., da Silva, A., 2023. Influence of local scale and oceanic teleconnections on regional fire danger and wildfire trends. *Sci. Total Environ.* 883, 163397 <https://doi.org/10.1016/j.scitotenv.2023.163397>.
- Jyoteeshkumar Reddy, P., Perkins-Kirkpatrick, S.E., Sharples, J.J., 2021a. Intensifying Australian heatwave trends and their sensitivity to observational data. *Earth's Future* 9 (4). <https://doi.org/10.1029/2020EF001924>.
- Jyoteeshkumar Reddy, P., Sharples, J.J., Lewis, S.C., Perkins-Kirkpatrick, S.E., 2021b. Modulating influence of drought on the synergy between heatwaves and dead fine fuel moisture content of bushfire fuels in the Southeast Australian region. *Weather Clim. Extr.* 31, 100300 <https://doi.org/10.1016/j.wace.2020.100300>.
- Kendall, M.G., 1948. *Rank Correlation Methods*. Oxford University Press, New York.
- Kim, S., 2015. ppcor: an R package for a fast calculation to semi-partial correlation coefficients. *Commun. Stat. Appl. Methods* 22 (6), 665–674. <https://doi.org/10.5351/CSAM.2015.22.6.665>.
- Kobayashi, S., Ota, Y., Harada, Y., Ebata, A., Moriya, M., Onoda, H., et al., 2015. The JRA-55 reanalysis: general specifications and basic characteristics. *J. Meteorol. Soc. Jpn.* 93 (1), 5–48. <https://doi.org/10.2151/jmsj.2015-001>.
- Kogan, F., Powell, A., Fedorov, O., 2011. *Use of Satellite and In-Situ Data to Improve Sustainability*. Springer, Netherlands, Dordrecht.
- Kogan, F., Salazar, L., Royzman, L., 2012. Forecasting crop production using satellite-based vegetation health indices in Kansas, USA. *Int. J. Remote Sens.* 33 (9), 2798–2814. <https://doi.org/10.1080/0143161.2011.621464>.
- Kogan, F., Adamenko, T., Guo, W., 2013. Global and regional drought dynamics in the climate warming era. *Remote Sens. Lett.* 4 (4), 364–372. <https://doi.org/10.1080/2150704X.2012.736033>.
- Kogan, F.N., 1990. Remote sensing of weather impacts on vegetation in non-homogeneous areas. *Int. J. Remote Sens.* 11 (8), 1405–1419. <https://doi.org/10.1080/01431690895102>.
- Lau, N.-C., Nath, M.J., 2014. Model simulation and projection of European heat waves in present-day and future climates. *J. Clim.* 27 (10), 3713–3730. <https://doi.org/10.1175/JCLI-D-13-00284.1>.
- Liu, Y., San Liang, X., Weisberg, R.H., 2007. Rectification of the bias in the wavelet power spectrum. *J. Atmos. Ocean. Technol.* 24 (12), 2093–2102. <https://doi.org/10.1175/2007JTECH0511.1>.
- Liu, Y., Huang, X., Yang, Q., Cao, Y., 2021. The turning point between urban vegetation and artificial surfaces for their competitive effect on land surface temperature. *J. Clean. Prod.* 292, 126034 <https://doi.org/10.1016/j.jclepro.2021.126034>.

- Mann, H.B., 1945. Nonparametric tests against trend. *Econometrica* 13 (3), 245. <https://doi.org/10.2307/1907187>.
- Mateus, P., Fernandes, P.M., 2014. Forest fires in Portugal: dynamics, causes and policies. In: *Forest Context and Policies in Portugal*. Springer, Cham, pp. 97–115.
- Matsuyama, H., Watanabe, T., Zemtsov, V., 2023. Extreme drought around Tomsk, Russia in summer 2012 in comparison with other regions in Western Siberia. *Water* 15 (3), 388. <https://doi.org/10.3390/w15030388>.
- Miralles, D.G., Teuling, A.J., van Heerwaarden, C.C., Vilà-Guerau de Arellano, J., 2014. Mega-heatwave temperatures due to combined soil desiccation and atmospheric heat accumulation. *Nat. Geosci.* 7 (5), 345–349. <https://doi.org/10.1038/ngeo2141>.
- Morales, M.S., Cook, E.R., Barichivich, J., Christie, D.A., Villalba, R., LeQuesne, C., et al., 2020. Six hundred years of South American tree rings reveal an increase in severe hydroclimatic events since mid-20th century. *Proc. Natl. Acad. Sci. U. S. A.* 117 (29), 16816–16823. <https://doi.org/10.1073/pnas.2002411117>.
- Mukhawana, M.B., Kanyerere, T., Kahler, D., 2023. Review of in-situ and remote sensing-based indices and their applicability for integrated drought monitoring in South Africa. *Water* 15 (2), 240. <https://doi.org/10.3390/w15020240>.
- Nairn, J., Fawcett, R., 2013. Defining heatwaves: heatwave defined as a heat-impact event servicing all community and business sectors in Australia.
- Nairn, J., Ostendorf, B., Bi, P., 2018. Performance of excess heat factor severity as a global heatwave health impact index. *Int. J. Environ. Res. Public Health* 15 (11). <https://doi.org/10.3390/ijerph15112494>.
- National Geographic. Understanding drought. <https://www.nationalgeographic.org/article/understanding-drought/> (accessed 09/30/2023).
- Ndehedehe, C.E., Adeyeri, O.E., Onojeghuo, A.O., Ferreira, V.G., Kalu, I., Okwuashi, O., 2023a. Understanding global groundwater-climate interactions. *Sci. Total Environ.* 904, 166571. <https://doi.org/10.1016/j.scitotenv.2023.166571>.
- Ndehedehe, C.E., Ferreira, V.G., Adeyeri, O.E., Correa, F.M., Usman, M., Oussou, F.E., et al., 2023b. Global assessment of drought characteristics in the Anthropocene. *Resour. Environ. Sustain.* 12, 100105. <https://doi.org/10.1016/j.resenv.2022.100105>.
- Ng, E.K.W., Chan, J.C.L., 2012. Geophysical applications of partial wavelet coherence and multiple wavelet coherence. *J. Atmos. Ocean. Technol.* 29 (12), 1845–1853. <https://doi.org/10.1175/JTECH-D-12-00056.1>.
- Nugraha, A.S.A., Kamal, M., Murti, S.H., Widyatmanti, W., 2023. Development of the triangle method for drought studies based on remote sensing images: a review. *Remote Sens. Appl. Soc. Environ.* 29, 100920. <https://doi.org/10.1016/j.rsase.2023.100920>.
- O'Neill, B.C., Tebaldi, C., van Vuuren, D.P., Eyring, V., Friedlingstein, P., Hurtt, G., et al., 2016. The Scenario Model Intercomparison Project (ScenarioMIP) for CMIP6. *Geosci. Model Dev.* 9 (9), 3461–3482. <https://doi.org/10.5194/gmd-9-3461-2016>.
- Ossola, A., Jenerette, G.D., McGrath, A., Chow, W., Hughes, L., Leishman, M.R., 2021. Small vegetated patches greatly reduce urban surface temperature during a summer heatwave in Adelaide, Australia. *Landscape Urban Plan.* 209, 104046. <https://doi.org/10.1016/j.landurbplan.2021.104046>.
- Parete, J., Amraoui, M., Menezes, I., Pereira, M.G., 2019. Drought in Portugal: current regime, comparison of indices and impacts on extreme wildfires. *Sci. Total Environ.* 685, 150–173. <https://doi.org/10.1016/j.scitotenv.2019.05.298>.
- Pausas, J.G., Paula, S., 2012. Fuel shapes the fire-climate relationship: evidence from Mediterranean ecosystems. *Glob. Ecol. Biogeogr.* 21 (11), 1074–1082. <https://doi.org/10.1111/j.1466-8238.2012.00769.x>.
- Pei, F., Wu, C., Liu, X., Li, X., Yang, K., Zhou, Y., et al., 2018. Monitoring the vegetation activity in China using vegetation health indices. *Agric. For. Meteorol.* 248, 215–227. <https://www.sciencedirect.com/science/article/pii/s0168192317303210>.
- Penuelas, J., Sardans, J., Filella, I., Estiarte, M., Llusia, J., Ogaya, R., et al., 2017. Impacts of global change on Mediterranean forests and their services. *Forests* 8 (12), 463. <https://doi.org/10.3390/f8120463>.
- Pérez-Invernón, F.J., Gordillo-Vázquez, F.J., Huntrieser, H., Jöckel, P., 2023. Variation of lightning-ignited wildfire patterns under climate change. *Nat. Commun.* 14 (1), 739. <https://www.nature.com/articles/s41467-023-36500-5>.
- Perkins, S.E., Alexander, L.V., 2013. On the measurement of heat waves. *J. Clim.* 26 (13), 4500–4517. <https://doi.org/10.1175/JCLI-D-12-00383.1>.
- Perkins, S.E., Argüeso, D., White, C.J., 2015. Relationships between climate variability, soil moisture, and Australian heatwaves. *J. Geophys. Res.* 120 (16), 8144–8164. <https://doi.org/10.1002/2015JD023592>.
- Perkins-Kirkpatrick, S.E., Lewis, S.C., 2020. Increasing trends in regional heatwaves. *Nat. Commun.* 11 (1), 3357. <https://doi.org/10.1038/s41467-020-16970-7>.
- Pincetl, S., Gillespie, T.W., Pataki, D.E., Porse, E., Jia, S., Kidera, E., et al., 2019. Evaluating the effects of turf-replacement programs in Los Angeles. *Landscape Urban Plan.* 185, 210–221. <https://doi.org/10.1016/j.landurbplan.2019.01.011>.
- Pinzon, J., Tucker, C., 2014. A non-stationary 1981–2012 AVHRR NDVI3g time series. *Remote Sens.* 6 (8), 6929–6960. <https://doi.org/10.3390/rs6086929>.
- Rayner, N.A., 2003. Global analyses of sea surface temperature, sea ice, and night marine air temperature since the late nineteenth century. *J. Geophys. Res.* 108 (D14). <https://doi.org/10.1029/2002JD002670>.
- Reichstein, M., Bahn, M., Ciais, P., Frank, D., Mahecha, M.D., Seneviratne, S.I., et al., 2013. Climate extremes and the carbon cycle. *Nature* 500 (7462), 287–295. <https://doi.org/10.1038/nature12350>.
- Richardson, D., Black, A.S., Irving, D., Matear, R.J., Monselesan, D.P., Risbey, J.S., et al., 2022. Global increase in wildfire potential from compound fire weather and drought. *npj Clim. Atmos. Sci.* 5 (1) <https://doi.org/10.1038/s41612-022-00248-4>.
- Saft, M., Western, A.W., Zhang, L., Peel, M.C., Potter, N.J., 2015. The influence of multiyear drought on the annual rainfall-runoff relationship: an Australian perspective. *Water Resour. Res.* 51 (4), 2444–2463. <https://doi.org/10.1002/2014WR015348>.
- Schulzweida, U., 2022. CDO User Guide.
- Sen, P.K., 1968. Estimates of the regression coefficient based on Kendall's tau. *J. Am. Stat. Assoc.* 63 (324), 1379–1389. <https://doi.org/10.1080/01621459.1968.10480934>.
- Seneviratne, S.I., Lüthi, D., Litschi, M., Schär, C., 2006. Land-atmosphere coupling and climate change in Europe. *Nature* 443 (7108), 205–209. <https://doi.org/10.1038/nature05095>.
- Sheffield, J., Wood, E.F., Roderick, M.L., 2012. Little change in global drought over the past 60 years. *Nature* 491 (7424), 435–438. <https://doi.org/10.1038/nature11575>.
- Sherwood, S.C., Huber, M., 2010. An adaptability limit to climate change due to heat stress. *Proc. Natl. Acad. Sci. U. S. A.* 107 (21), 9552–9555. <https://doi.org/10.1073/pnas.0913352107>.
- Steadman, R.G., 1979. The assessment of sultriness. Part I: a temperature-humidity index based on human physiology and clothing science. *J. Appl. Meteorol.* 18 (7), 861–873. [https://doi.org/10.1175/1520-0450\(1979\)018<0861:TAOSPI>2.0.CO;2](https://doi.org/10.1175/1520-0450(1979)018<0861:TAOSPI>2.0.CO;2).
- Teixeira, E.I., Fischer, G., van Velthuizen, H., Walter, C., Ewert, F., 2013. Global hotspots of heat stress on agricultural crops due to climate change. *Agric. For. Meteorol.* 170, 206–215. <https://doi.org/10.1016/j.agrformet.2011.09.002>.
- Theil, H., 1992. A rank-invariant method of linear and polynomial regression analysis. In: Hallet, A.J.H., Marquez, J. (Eds.), *Henri Theil's Contributions to Economics and Econometrics: Econometric Theory and Methodology*. Springer, Netherlands, Dordrecht, pp. 345–381.
- Torrence, C., Webster, P.J., 1999. Interdecadal changes in the ENSO–monsoon system. *J. Clim.* 12 (8), 2679–2690. [https://journals.ametsoc.org/view/journals/clim/12/8/1520-0442.1999.012\\_2679.icitem\\_2.0.co\\_2.xml](https://journals.ametsoc.org/view/journals/clim/12/8/1520-0442.1999.012_2679.icitem_2.0.co_2.xml).
- Trenberth, K.E., Dai, A., van der Schrier, G., Jones, P.D., Barichivich, J., Briffa, K.R., et al., 2014. Global warming and changes in drought. *Nat. Clim. Chang.* 4 (1), 17–22. <https://doi.org/10.1038/nclimate2067>.
- Udmale, P.D., Ichikawa, Y., Manandhar, S., Ishidaira, H., Kiem, A.S., Shaowei, N., et al., 2015. How did the 2012 drought affect rural livelihoods in vulnerable areas? Empirical evidence from India. *Int. J. Disaster Risk Reduct.* 13, 454–469. <https://doi.org/10.1016/j.ijdrr.2015.08.002>.
- van Dijk, A.I.J.M., Beck, H.E., Crosbie, R.S., Jeu, R.A.M. de, Liu, Y.Y., Podger, G.M., et al., 2013. The Millennium Drought in southeast Australia (2001–2009): natural and human causes and implications for water resources, ecosystems, economy, and society. *Water Resour. Res.* 49 (2), 1040–1057. <https://doi.org/10.1002/wrcr.20123>.
- van Vuuren, D.P., Edmonds, J., Kainuma, M., Riahi, K., Thomson, A., Hibbard, K., et al., 2011. The representative concentration pathways: an overview. *Clim. Chang.* 109 (1–2), 5–31. <https://doi.org/10.1007/s10584-011-0148-z>.
- Veleda, D., Montagne, R., Araujo, M., 2012. Cross-wavelet bias corrected by normalizing scales. *J. Atmos. Ocean. Technol.* 29 (9), 1401–1408. <https://doi.org/10.1175/JTECH-D-11-00140.1>.
- Vicente-Serrano, S.M., Beguería, S., López-Moreno, J.I., 2010a. A multiscalar drought index sensitive to global warming: the standardized precipitation evapotranspiration index. *J. Clim.* 23 (7), 1696–1718. <https://doi.org/10.1175/2009CLJ2909.1>.
- Vicente-Serrano, S.M., Beguería, S., López-Moreno, J.I., Angulo, M., El Kenawy, A., 2010b. A new global 0.5° gridded dataset (1901–2006) of a multiscalar drought index: comparison with current drought index datasets based on the palmer drought severity index. *J. Hydrometeorol.* 11 (4), 1033–1043. <https://doi.org/10.1175/2010JHM1224.1>.
- Weng, Z., Niu, J., Guan, H., Kang, S., 2023. Three-dimensional linkage between meteorological drought and vegetation drought across China. *Sci. Total Environ.* 859 (Pt 2), 160300. <https://doi.org/10.1016/j.scitotenv.2022.160300>.
- Wild, M., Gilgen, H., Roesch, A., Ohmura, A., Long, C.N., Dutton, E.G., et al., 2005. From dimming to brightening: decadal changes in solar radiation at Earth's surface. *Science (New York, N.Y.)* 308 (5723), 847–850. <https://doi.org/10.1126/science.1103215>.
- Wilhite, D.A., Glantz, M.H., 1985. Understanding: the drought phenomenon: the role of definitions. *Water Int.* 10 (3), 111–120. <https://doi.org/10.1080/02508068508686328>.
- Wondmagegn, B.Y., Xiang, J., Dear, K., Williams, S., Hansen, A., Pisaniello, D., et al., 2021. Impact of heatwave intensity using excess heat factor on emergency department presentations and related healthcare costs in Adelaide, South Australia. *Sci. Total Environ.* 781, 146815. <https://doi.org/10.1016/j.scitotenv.2021.146815>.
- Yang, W., Guo, W., Kogan, F., 2018. VIIRS-based high resolution spectral vegetation indices for quantitative assessment of vegetation health: second version. *Int. J. Remote Sens.* 39 (21), 7417–7436. <https://doi.org/10.1080/01431161.2018.1470701>.
- Yang, W., Kogan, F., Guo, W., 2020. An ongoing blended long-term vegetation health product for monitoring global food security. *Agronomy* 10 (12), 1936. <https://doi.org/10.3390/agronomy10121936>.
- Yu, Y., Mao, J., Wullschleger, S.D., Chen, A., Shi, X., Wang, Y., et al., 2022. Machine learning-based observation-constrained projections reveal elevated global socioeconomic risks from wildfire. *Nat. Commun.* 13 (1), 1250. <https://doi.org/10.1038/s41467-022-28853-0>.
- Zhao, L., Dai, A., Dong, B., 2018. Changes in global vegetation activity and its driving factors during 1982–2013. *Agric. For. Meteorol.* 249, 198–209. <https://doi.org/10.1016/j.agrformet.2017.11.013>.
- Zhao, Z., Lin, Z., Li, F., Rogers, B.M., 2022. Influence of atmospheric teleconnections on interannual variability of Arctic-boreal fires. *Sci. Total Environ.* 838 (Pt 4), 156550. <https://doi.org/10.1016/j.scitotenv.2022.156550>.
- Zhou, L., Tian, Y., Myneni, R.B., Ciais, P., Saatchi, S., Liu, Y.Y., et al., 2014. Widespread decline of Congo rainforest greenness in the past decade. *Nature* 509 (7498), 86–90. <https://doi.org/10.1038/nature13265>.